CHEMISTRY OF MATERIALS

pubs.acs.org/cm

Article

Slab-Gliding–Induced Structural Evolution in β-V_2O_5 Enables Reversible High Na-Ion Storage: A Combined *Operando* Synchrotron Diffraction and *Operando* XAS Study

Rafael Córdoba,* Jakub Goclon, Angelina Sarapulova, Julia Maibach, Sonia Dsoke, Ester García-González, François Fauth, Alois Kuhn, and Flaviano García-Alvarado

Cite This: *Chem. Mater.* 2025, 37, 8649–8663

Read Online

ACCESS | Metrics & More | Article Recommendations | Supporting Information

ABSTRACT: High-pressure β-V_2O_5 is a positive electrode material for sodium-ion batteries offering a remarkable high capacity of ~150 mAh g^{-1}. Despite its attractive electrochemical properties and interesting crystal chemistry due to the existence of several sodiated phases, the sodium intercalation mechanism that provides reversible insertion is still largely unclear. In this work, we conducted a comprehensive investigation of the structural evolution, oxidation state and local structural changes of high-pressure β-V_2O_5 during sodium intercalation. *Operando* synchrotron diffraction and *operando* X-ray absorption spectroscopy together with X-ray photoelectron spectroscopy, reveal the reversibility of sodium (de)-intercalation and allowed us to gain a complete picture of the crystal structure evolution and oxidation state changes during cycling. A full crystal structure determination of the sodiated phases $Na_xV_2O_5$ ($0 \leq x \leq 1$) was performed for the first time directly from *operando* synchrotron diffraction and *ex situ* transmission electron microscopy. Our findings reveal a fully reversible phase transition sequence, $P2_1/m \rightarrow C2/m \rightarrow P2_1/m$, during sodium intercalation, driven by the facile slab-gliding of V_2O_5 layers along the crystallographic *b* direction to accommodate varying amounts of sodium ions. This storage mechanism was further supported with first-principles density functional theory (DFT) calculations.

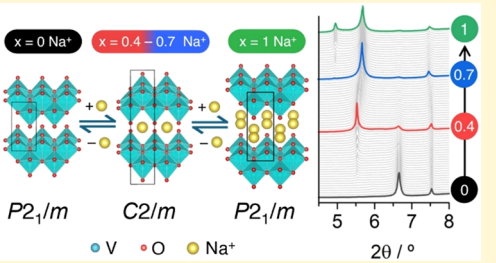

1. INTRODUCTION

Vanadium pentoxide, V_2O_5, is a polyvalent compound with a wide range of applications, including heterogeneous catalysis,[1] electrochromic devices[2] or electrochemical energy storage.[3] This versatility arises from its rich redox chemistry and polymorphism. Its thermodynamically most stable polymorph, α-V_2O_5, exhibits electrochemical activity due to its layered structure, which allows mobile species to intercalate within the interlayer spacing accompanied by reduction of V^{5+}. α-V_2O_5 has an orthorhombic structure composed of sheets of VO_5 square pyramids piled up along the *c*-axis, held together by van der Waals forces. Precisely, layered compounds with van der Waals interlayer spacing are strong candidates for positive/negative electrode materials, as their host lattices help mitigate structural distortions during metal ion (de)intercalation reactions, a key to preserving cycle life in electrochemical cells. Due to these properties, α-V_2O_5 was identified in the 1970s as an attractive positive electrode material for lithium-ion batteries (LIBs).[4] Although the interlayer spacing (d = 4.37 Å) in α-V_2O_5 is sufficient for lithium (de)insertion,[5] it is less accommodating for larger sodium ions, making commercial V_2O_5 electrochemically inactive.[6] To achieve acceptable electrochemical activity, V_2O_5 must first be electrochemically transformed into the α'-NaV_2O_5 phase through the intercalation of one Na^+ ion,[6] or synthesized using alternative methods that yield modified V_2O_5 structures, like xerogels[7] or nanosized V_2O_5.[8]

A common soft chemistry approach for synthesizing stable V_2O_5 polymorphs involves chemically extracting metal ions (M = Li, Na, Cu, Ag, etc.) from vanadium bronzes $M_xV_2O_5$ while preserving the V–O framework. Additionally, ion extraction enhances specific capacity by reducing molecular weight and creating vacancies that facilitate ion mobility. This approach has been widely used to obtain new V_2O_5 polymorphs. García-Alvarado et al. synthesized the three-dimensional β'-V_2O_5 and layered ε'-V_2O_5 by extracting Cu from β-$Cu_{0.55}V_2O_5$ and ε-$Cu_{0.9}V_2O_5$, respectively.[9,10] A similar method involves removing Li from γ-LiV_2O_5 to obtain γ'-V_2O_5.[11] Several of these polymorphs exhibit interesting electrochemical performance as positive electrodes for sodium-ion batteries (NIBs). Renard et al.[12] reported a reversible capacity of 60–80 mAh g^{-1} for γ'-V_2O_5 at 3.3. V vs Na^+/Na, 1.5 V higher than α-V_2O_5.[13] This capacity nearly doubles (120 mAh g^{-1}) upon

Received: June 16, 2025
Revised: September 9, 2025
Accepted: October 3, 2025
Published: October 31, 2025

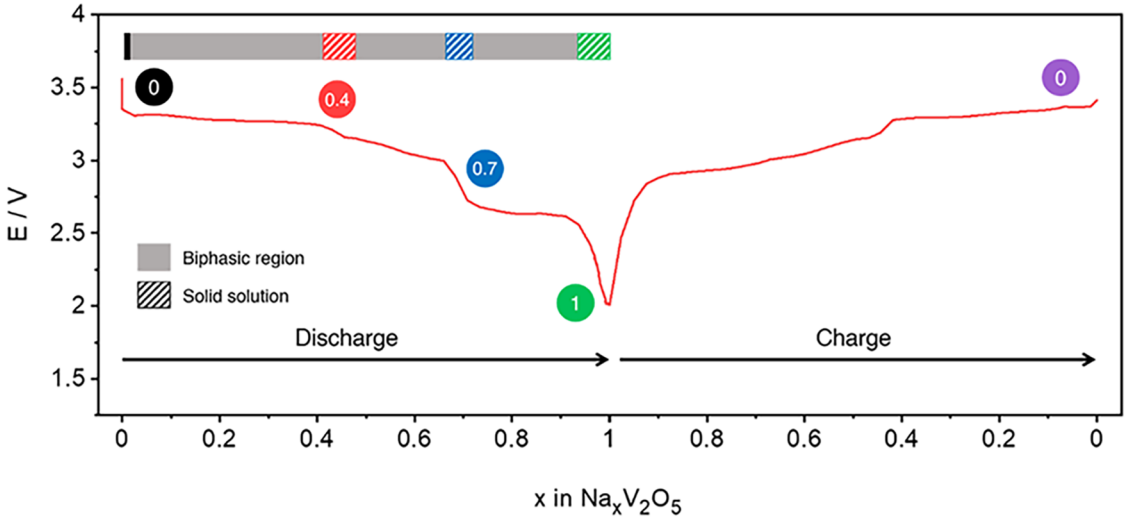

Figure 1. Equilibrium voltage-composition curve (GITT experiment from ref. 23) for sodium (de)intercalation in β-V_2O_5 in the sodium compositional range $0 \leq x \leq 1$. The horizontal bar (top of the figure) describes the nature of the observed intercalation mechanism. Selected compositions belonging to different single-phase regions are highlighted with colored circles: pristine β-V_2O_5—black, $Na_{0.4}V_2O_5$—red, $Na_{0.7}V_2O_5$—blue, NaV_2O_5—green, β-V_2O_5 after full charge—purple. This identification color will be used throughout the entire work.

nanosizing.[14] Meanwhile, ε'-V_2O_5 carbon nanotube composite delivers 200 mAh g^{-1} after 50 cycles at a C/10 rate, with an average potential of 2.8 V vs Na^+/Na.[14] Notably, β-V_2O_5, which cannot be synthesized at ambient pressure using conventional methods, is obtained at high-pressure.[15] High-pressure synthesis is a valuable route in solid-state chemistry for obtaining new polymorphs, often inducing structural transformations.[16−21] β-V_2O_5 is a promising cathode material for Li-,[22] Na-,[23] K-[24] and Mg-ion[25] storage. We previously demonstrated its outstanding Na intercalation properties achieving the theoretical capacity of 147 mAh g^{-1} (1 Na^+ per formula unit, f.u.),[23] in the 3.6−2 V voltage range vs Na^+/Na (Figure 1). Galvanostatic Intermittent Titration Technique (GITT) identified three sodiated $Na_xV_2O_5$ solid-solution single phases during progressive Na^+ intercalation.[23] These phases are separated from each other by corresponding two-phase regions and associated with the following sodium compositional ranges: x = 0.4−0.45, x = 0.67−0.72 and x = 0.95−1. For this study, we have selected representative compositions of the three regions: $Na_{0.4}V_2O_5$, $Na_{0.7}V_2O_5$ and NaV_2O_5 phases (Figure 1). The similarity of the *ex situ* X-ray diffraction (XRD) patterns of $Na_{0.4}V_2O_5$ and $Na_{0.7}V_2O_5$[23] is a clear indication of the close structural relationship between both phases over the entire compositional range x = 0.4−0.7.

Our previous work[26] examined the initial phase transformation of β-V_2O_5 to $Na_{0.4}V_2O_5$ using *operando* synchrotron XRD. However, to fully understand the reversible sodium intercalation in β-V_2O_5, the electrochemical Na storage mechanism in the entire compositional range $0 \leq x \leq 1$ needs to be investigated. This requires deciphering the structures of all sodiated $Na_xV_2O_5$ phases, and the atomic positions of V, O, and Na^+ guest ions, as well as the evolution of the vanadium oxidation state and local structure. *Operando* synchrotron diffraction is a highly powerful technique for investigating the structural changes in battery materials,[27] aimed at gaining a deeper understanding of the structural evolution of a battery material in real time. Furthermore, *operando* X-ray Absorption Spectroscopy (XAS) is another valuable technique for revealing the local structure and oxidation state during the electrochemical reaction. To the best of our knowledge, *operando* techniques have not yet been extensively used to study the reaction mechanism of β-V_2O_5 in sodium-ion batteries in detail. In this study, we investigated the evolution of the crystal structure of β-V_2O_5 during sodium intercalation in the $0 \leq x \leq 1$ range by *operando* synchrotron X-ray diffraction (SXRD) and high-resolution transmission electron microscopy, supported by density functional theory (DFT) calculations and migration paths analysis. The associated redox chemistry was investigated in detail using *operando* X-ray absorption spectroscopy (XAS) and *ex situ* X-ray photoelectron spectroscopy (XPS), providing insights into vanadium oxidation states and local structure. Additionally, we discuss the impact of increasing sodium content on sodium diffusion coefficient.

2. EXPERIMENTAL SECTION

2.1. Synthesis. For synthesis of β-V_2O_5, a previously dried sample of α-V_2O_5 (180 °C, 18 h) (Aldrich, 99.9%) was subjected to a high-pressure high-temperature treatment in a belt-type press (800 °C and 40 kbar for 30 min) as previously reported.[23] Sodiated samples for *ex situ* characterization were obtained by electrochemical methods as described in the sections below.

2.2. BET Method. Adsorption−desorption nitrogen experiments (BET method) required for the calculation of sodium diffusion coefficient were performed at 77 K in a Micromeritics ASAP 2020 analyzer. Samples were previously outgassed for 24 h at 110 °C under vacuum (2 μmHg).

2.3. Electrochemical Tests. Galvanostatic discharge−charge cycling experiments were carried out in sodium half-cells, composed of the positive electrode, a glass fiber separator (Whatman) soaked in 1 M $NaClO_4$ ethylene carbonate (EC): propylene carbonate (PC) (1:1 v/v) electrolyte, and sodium metal as the counter/reference negative electrode. The positive electrode was prepared by mixing β-V_2O_5, conductive carbon Super C65 (Timcal), and poly(vinylidene fluoride) (PVDF, Kynarflex) binder in an 8:1:1 weight ratio using *N*-methyl-2-pyrrolidone (NMP, Sigma-Aldrich) as solvent (1 mL of NMP per 300 mg of powder mix) during 24 h. The slurry was cast on aluminum foil (15 μm thickness, Gelon) with a wet coating thickness of 105 μm, from where 8 mm diameter disks were punched out. The electrodes, with an average mass loading of the active material of ∼3 mg, were then dried under vacuum at 80 °C for 12 h. Cells were assembled in an argon-filled glovebox (H_2O and O_2 < 0.1 ppm). The

https://doi.org/10.1021/acs.chemmater.5c01520
Chem. Mater. 2025, 37, 8649−8663

type of cell used for each electrochemical test will be mentioned in the following sections.

For crystal structure analysis using HRTEM, two sodium-intercalated $Na_xV_2O_5$ materials with different sodium content were electrochemically synthesized. Due to the predicted similarity of $Na_xV_2O_5$ structures in the $x = 0.4-0.7$ composition range, a sample having $x = 0.5$ was targeted, together with a fully sodium intercalated sample with $x = 1$. For this purpose, sodium half-cells (CR2032 coin cells) bearing β-V_2O_5 as positive electrode were discharged at C/20 (corresponding to the intercalation of 1 Na^+ per formula unit in 20 h and equivalent to 7.3 mA g^{-1}) to fixed potential values whose composition and potential values were selected from the GITT curve shown in Figure 1. Cells were held potentiostatically at the fixed potentials of 3.1 V (from this point onward, all voltage values are given vs Na^+/Na) for $Na_{0.5}V_2O_5$, and 2.0 V for NaV_2O_5, until the residual current was $<10^{-4}$ mA or <0.01% of the initial current. In the case of *ex situ* XPS, four samples were prepared electrochemically using the same procedure. The fixed potentials and compositions were the following: 3.1 V for $Na_{0.4}V_2O_5$, 2.75 V for $Na_{0.7}V_2O_5$, 2.0 V for NaV_2O_5 and 3.6 V for charged β-V_2O_5. Afterward, positive electrodes were removed from the cells inside an argon-filled glovebox and rinsed with PC to eliminate any residual electrolyte. The electrodes were transferred under argon atmosphere to the microscope for HRTEM and the spectrometer for XPS.

For Potentiostatic Electrochemical Impedance Spectroscopy (PEIS) experiments, three-electrode Swagelok cells were employed to analyze the cathode contribution separately. Separate disks of sodium metal acted as counter and reference electrodes. Impedance data were collected in the 1 MHz−10 mHz frequency range, applying a 10 mV AC perturbation. The procedure consisted of discharging the cell at C/20 (7.3 mA g^{-1}) to the corresponding potential for each phase (shown above), followed by a 3 h potentiostatic hold period, performing the PEIS measurement, and (dis)charging again to the next potential to repeat the process. Fitting of PEIS spectra and equivalent circuit modeling were carried out through Z-Fit (EC-Lab software).

CR2032 coin cells were used for Potentiostatic Intermitent Titration Technique (PITT) and GITT experiments required for the calculation of sodium diffusion coefficient. In PITT experiments, the cell was discharged with steps of 10 mV every 8 h in the 3.6−2 V potential range. In the case of GITT, each step consisted of a discharge at C/20 (7.3 mA g^{-1}) applied for 30 min in the same potential window, followed by a 4 h rest period. All electrochemical experiments were performed using a VMP3 Biologic battery tester.

2.4. *Operando* Synchrotron Diffraction (SXRD). *Operando* diffraction during cycling was performed at the Material Science and Powder Diffraction beamline (MSPD) at ALBA synchrotron light facility (Barcelona, Spain).[28] The *in situ* cells for SXRD were assembled using 2032-type coin cells, with a 5 mm diameter beam entrance covered with Kapton windows.[27] The cathode material (a mixture of V_2O_5, Super C65 conductive carbon and PVDF binder with a ratio of 8:1:1, in total ∼10 mg) was prepared by pressing the mixture onto an aluminum mesh within a 5 mm hole in the center. This setup ensures that only the V_2O_5 material is detected during the *operando* synchrotron measurements. *Operando* synchrotron diffraction patterns were collected at room temperature in transmission geometry, with the beam going through all the components of the *in situ* cell, and $\lambda = 0.8263$ Å wavelength (15 keV), selected by means of a double-crystal Si(111) monochromator, and using the position sensitive 1-D detector MYTHEN. Data were collected with an effective exposure time of 60 s every 6 min, in the 5−50° 2θ angular range, during a full galvanostatic discharge−charge cycle at C/17 (8.6 mA g^{-1}) in the 3.6−2.0 V vs Na^+/Na potential range. To improve powder averaging (increase of the number of contributing crystallites), the coin cells were continuously oscillated by ±5° around the incoming beam direction.

The diffraction data analysis was carried out using the Rietveld method with the Fullprof software package.[29] For Rietveld refinements, the Na occupancy was determined and fixed based on the charge and capacity obtained from the electrochemical data, *i.e.*, x in $Na_xV_2O_5$, which was recorded by EC-Lab software for each diffraction pattern. The positions of the Na ions were clarified using Bond Valence Sum Difference Maps (BVS-DM), as explained in more detail in the Supporting Information. BVS maps were obtained utilizing the BVS Mapping package incorporated in Fullprof.[29] Difference maps (DMs) and structural models were visualized using the Vesta 3.3 software.[30]

2.5. High-Resolution Transmission Electron Microscopy (HRTEM). Samples were ultrasonically dispersed in *n*-butanol and transferred to a carbon-coated copper grid. Selected Area Electron Diffraction (SAED) and high-resolution transmission electron microscopy (HRTEM) were performed on a JEOL JEM GRAND ARM 300cFEG electron microscope with corrected aberration in the objective lens and working at 300 kV (point resolution of 0.05 nm); and on a JEOL JEM 2000FX transmission microscope operating at 200 kV (point resolution of 0.31 nm). Scanning electron microscopy on the pristine powder was performed using a JEOL JSM-6400 microscope.

2.6. *Operando* Hard X-ray Absorption Spectroscopy (Hard-XAS). Experiments were carried out at the beamline P65 at DESY synchrotron facilities.[31] The cell configuration was the same as in *operando* SXRD. Vanadium XAS spectra were collected every 6 min in fluorescence geometry using a passivated implanted planar silicon (PIPS) diode in the 5315−6065 eV energy range. The V K-edge (energy range: 5450−5500 eV) for β-V_2O_5 was analyzed during a complete galvanostatic discharge/charge cycle in the 3.6−2 V potential range, performed at C/20 in the previously described *in situ* cell. Vanadium foil was employed for calibrating the energy, whereas VO_2 and V_2O_5 were used as standard materials. All the data were collected at room temperature with a Si(111) double crystal monochromator, and processed by means of the DEMETER software package.[32]

2.7. X-ray Photoelectron Spectroscopy (XPS). *Ex situ* X-ray photoelectron spectroscopy was performed employing a K-Alpha instrument (Thermo Fisher Scientific), applying a microfocused, monochromatic Al K-alpha X-ray source (1486.7 eV) with 400-μm spot size. All the data were recorded using a pass energy of 50 eV for detailed analysis and 200 eV for survey spectra. Some samples required using the K-alpha charge compensation system using a combination of both electrons and low-energy argon ions. Data acquisition and processing, using the Thermo Avantage software, are reported in ref. 33. The metal oxide signal in the O 1*s* spectra at 530 eV was employed as a reference for the binding energy, while the overall binding energy scale was controlled using well-known photoelectron peaks of metallic Ag, Au, and Cu. The background (Smart background shape implemented in Avantage) was subtracted over the V 2*p* and O 1*s* binding energy range. The V $2p_{3/2}$ peak was fitted using symmetric Voigt profiles with a fixed Lorentzian contribution of 30%.

2.8. Computational Section. All Density Functional Theory (DFT) calculations were performed using the Quantum ESPRESSO package.[34] The exchange-correlation energy was described within the Generalized Gradient Approximation (GGA) functional of Perdew, Burke and Ernzerhof (PBE).[35] The Grimme's D3 semiempirical van der Waals correction was included to deal with dispersion interactions.[36] The effect of the core electrons was simulated by an ultrasoft pseudopotential.[37] The valence electrons were expanded in a plane-wave basis with a cutoff kinetic energy of 50 Ry for the wave functions and 500 Ry for the charge density. The convergence threshold for self-consistency was set to 10^{-8} Ry. The relaxation procedure was stopped when each Hellmann−Feynman force component was no greater than 10^{-2} eV $Å^{-1}$. In our previous paper,[26] we performed comprehensive DFT calculations for the β-V_2O_5 and $Na_{0.375}V_2O_5$ bulk. For the proper description of the electronic structure of β-V_2O_5, we adopted the DFT + U formulation by Dudarev et al.[38] as implemented by Cococcioni and de Gironcoli.[39] In order to reproduce the band gap of the β-V_2O_5 bulk, $U_{eff} = 4$ eV was used (see ref. 26). This value was also taken for modeling of $Na_xV_2O_5$ phases. The Brillouin zone was sampled using a $2 \times 6 \times 4$ Monkhorst−Pack[40] *k*-point grid. Spin-polarization was

https://doi.org/10.1021/acs.chemmater.5c01520
Chem. Mater. 2025, 37, 8649−8663

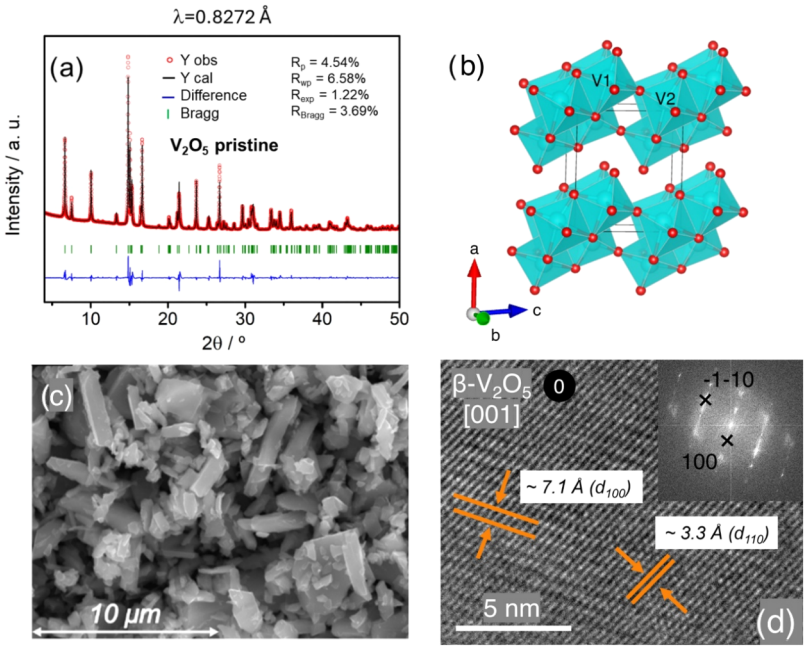

Figure 2. (a) Rietveld refinement from synchrotron diffraction data measured in capillary, (b) crystal structure (VO_6 octahedra—turquoise, oxygen—red), (c) SEM micrography and (d) HRTEM micrography oriented along [001] zone axis of pristine β-V_2O_5. Corresponding Fourier transform is shown as inset in Figure 2d. Indexation of the reflections has been done according to the S.G. $P2_1/m$.

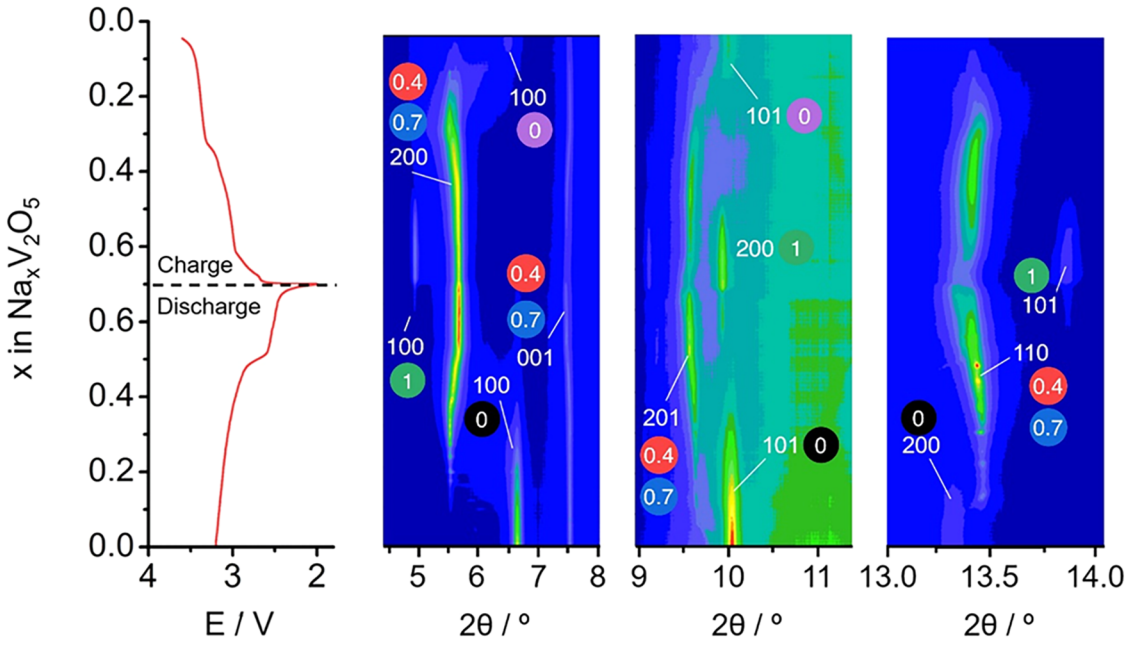

Figure 3. Contour maps of *operando* synchrotron diffraction of β-V_2O_5 collected during the first full discharge−charge cycle and the corresponding discharge−charge profile at C/17 in the voltage range 3.7−2.0 V. Reflections are indexed according to the unit cells of the respective $Na_xV_2O_5$ phases, and each reflection is annotated with its corresponding phase.

taken into account in each case. To identify the Na-ion migration barriers and the corresponding transition state (TS), the climbing image nudged elastic band (CI-NEB)[41,42] method was used. In order to model the migration paths, one Na atom was always removed within the supercell. Depending on the chosen path, we set different number of images between the initial and final configuration. The CI-NEB calculations were fully relaxed until the forces on the atoms were converged within 0.05 eV $Å^{-1}$. Due to the well-known problem of metastability of electronic states for GGA + U NEB calculations,[43−45] the standard GGA functional (PBE) was used. All the figures were produced using the visualization programs VESTA[30] and XcrySDen.[46]

3. RESULTS AND DISCUSSION

3.1. Structural Study. The synchrotron diffraction pattern of pristine β-V_2O_5 powder is displayed in Figure 2a, indicating a high crystallinity of the material. All reflections can be indexed in the monoclinic β-V_2O_5 structure model with space group $P2_1/m$, and the lattice parameters are a = 7.1140(2) Å, b = 3.5718(1) Å, c = 6.2846(2) Å and β = 90.07(1)°, in accordance with previously published work.[15,23] In contrast to orthorhombic α-V_2O_5, (space group, S.G. *Pmmn*), which exhibits five-coordinated VO_5 pyramids, V atoms in β-V_2O_5 are

https://doi.org/10.1021/acs.chemmater.5c01520
Chem. Mater. 2025, 37, 8649−8663

six-coordinated within distorted VO_6 octahedra. The β-V_2O_5 structure consists of quadruple units of edge-sharing bioctahedra sharing edges along the *b* direction. These chains are linked via corner-sharing bioctahedra along the *c* direction, resulting in a layered arrangement, with layers stacked along the *a* direction and held together by van der Waals forces (Figure 2b). SEM (Figure 2c) revealed that the V_2O_5 is composed of prisms of several micrometers in size. Transmission electron microscopy on the pristine β-V_2O_5 (Figure 2d) confirmed the structural results obtained from SXRD. As expected, crystals of β-V_2O_5 exhibit the characteristic 7.1 Å interlayer distance and its Fourier transform is in good agreement with the reciprocal space of $P2_1/m$ space group.

3.2. Electrochemical Mechanism of β-V_2O_5 in NIBs. The structural evolution of β-V_2O_5 during galvanostatic cycling in the 3.6−2.0 V potential range has been studied by *operando* SXRD. The Rietveld refinement of the V_2O_5 structure from data collected using the *in situ* cell in transmission geometry (Figure S1a, pattern no. 1) and *ex situ* data obtained in capillary (Figure 2a) showed a strong agreement, validating hereby the suitability of the *in situ* cell for acquiring highly reliable synchrotron diffraction data under *operando* conditions. Table S1 compares refinement results obtained for pristine V_2O_5 from data collected in capillary with those obtained using the *in situ* cell setup.

Diffraction patterns in selected angular regions of the first discharge−charge cycle of V_2O_5 vs Na are shown in Figure 3 as a contour plot. Overall, the amount of intercalated sodium in the *in situ* cell is lower than that observed in the GITT discharge curve displayed in Figure 1, indicating that equilibrium conditions were obviously not achieved under the dynamic galvanostatic discharge−charge conditions employed in the *operando* study. For clarity, we will refer to the idealized sodium compositions obtained from GITT in the remainder of this article.

Figure 4a shows a waterfall plot of the SXRD patterns collected upon sodium intercalation in β-V_2O_5 throughout the first discharge, in which selected compositions and corresponding diffraction patterns are highlighted. At the initial state of discharge, all the reflections are indexed based on the monoclinic β-V_2O_5 phase with space group $P2_1/m$ (see Rietveld refinement of pristine V_2O_5 in Figure S1a). In the beginning of the first discharge (Na intercalation), reflections of β-V_2O_5 progressively decrease in intensity and new reflections appear and increase in intensity, indicating that a two-phase reaction from β-V_2O_5 to $Na_{0.4}V_2O_5$ (phase region shown as red in GITT, Figure 1) occurs (region I in Figure 4a). The Na content of the newly formed phase at the end of the two-phase reaction (3.05 V) was estimated as $Na_{0.4}V_2O_5$ from GITT, with lattice parameters of a = 17.1623(8) Å, b = 3.5848(1) Å, c = 6.3024(1) Å, β = 86.29(1)°, according to the diffraction patterns and corresponding electrochemical profile (see the Rietveld refinement of $Na_{0.4}V_2O_5$ in Figure S1b, pattern no. 60). The discontinuous variation is very well observed by means of the 100 and 101 reflections at 6.6° and 10.1°, respectively, with respective new reflections at lower angles of 5.5° and 9.6° (Figures 3 and 4a). $Na_{0.4}V_2O_5$ also has a monoclinic structure and can be indexed with space group $C2/m$. The *C* centering involves doubling of the *a* parameter, along which the V_2O_5 layers are stacked, and while the interlayer spacing in β-V_2O_5 is represented by $\sim a$ (given that the β angle is close to 90°), it is $\sim a/2$ in $Na_{0.4}V_2O_5$ (Figure 4b and Table 1). Most notably, the significant shift of 100 to lower angles during the two-phase transition is linked to an increase of the interlayer spacing (aligned with the *a* direction) from 7.12 Å in β-V_2O_5 to 8.56 Å in $Na_{0.4}V_2O_5$ to accommodate Na^+ ions during sodium intercalation, while *b* and *c* parameters remain barely unchanged (Figure 4b and Table 1).

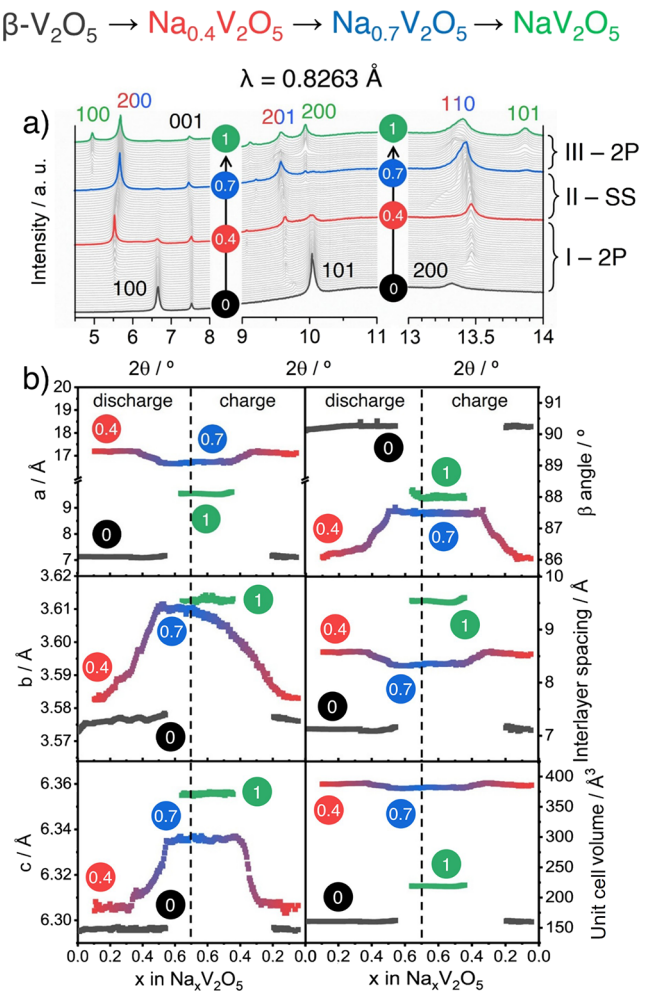

Figure 4. (a) Selected angular section of SXRD patterns collected during sodium intercalation (x = 1) in β-V_2O_5; (b) Unit cell parameters evolution upon sodium (de)intercalation of the different sodiated $Na_xV_2O_5$ phases. SS and 2P indicate solid-solution and biphasic transitions, respectively.

Upon further discharge beyond region I, the 200 reflection of $Na_{0.4}V_2O_5$ at 5.5° gradually shifts to higher angles, while 001, 201, and 110 at 7.5°, 9.6° and 13.4°, respectively, gradually shift to lower angles. The evolution seen in region II in Figure 4a indicates a solid-solution process between $Na_{0.4}V_2O_5$ and $Na_{0.7}V_2O_5$ (phase region shown in blue in GITT, Figure 1) at 2.8 V with a slight decrease of the unit cell. The Na content of the newly formed phase at the end of the solid-solution reaction at 2.8 V was estimated as $Na_{0.7}V_2O_5$ from GITT, with lattice parameters of a = 16.6951(6) Å, b = 3.6105(1) Å, c = 6.3351(1) Å, β = 87.56(1)°, according to the diffraction patterns and corresponding electrochemical profile (see the Rietveld refinement of $Na_{0.7}V_2O_5$ in Figure S1c, pattern no. 105). The underlying two-phase nature of the transition from $Na_{0.4}V_2O_5$ to $Na_{0.7}V_2O_5$ obtained from GITT is not resolved using *operando* synchrotron diffraction, performed under galvanostatically controlled conditions, due to the close structural similarity between the two phases.

https://doi.org/10.1021/acs.chemmater.5c01520
Chem. Mater. 2025, 37, 8649−8663

Table 1. Crystallographic Data for Selected Compositions in the β-$Na_xV_2O_5$ System Obtained from *Operando* SXRD Data

	discharge				charge		
space group	$P2_1/m$	$C2/m$	$C2/m$	$P2_1/m$	$C2/m$	$C2/m$	$P2_1/m$
phase	β-V_2O_5	$Na_{0.4}V_2O_5$	$Na_{0.7}V_2O_5$	NaV_2O_5	$Na_{0.7}V_2O_5$	$Na_{0.4}V_2O_5$	β-V_2O_5
a/Å	7.1211(1)	17.1623(8)	16.6951(6)	9.5437(1)	16.7383(5)	17.0846(7)	7.1041(1)
b/Å	3.5745(1)	3.5848(1)	3.6105(1)	3.6123(1)	3.6088(1)	3.5832(1)	3.5761(1)
c/Å	6.2902(1)	6.3024(1)	6.3351(1)	6.3546(1)	6.3354(1)	6.3065(1)	6.2958(1)
β/°	90.16(1)	86.29(1)	87.56(1)	88.26(1)	87.51(1)	86.06(1)	90.24(1)
interlayer spacing/Å	7.12	8.56	8.34	9.54	8.36	8.52	7.10
unit cell volume/Å^3	160.1	386.9	381.5	219.0	382.3	385.2	159.9

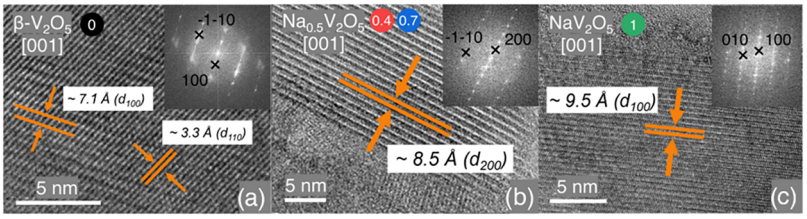

Figure 5. Micrographs of crystals of β-V_2O_5 (a), $Na_{0.5}V_2O_5$ (b) and NaV_2O_5 (c) oriented along the [001] zone axis. Corresponding Fourier transforms are shown as insets. Indexation of the reflections has been done in S.G. $P2_1/m$ for β-V_2O_5 and NaV_2O_5, and in S.G. $C2/m$ for $Na_{0.5}V_2O_5$. Selected compositions are highlighted with colored circles (with sodium content as deduced from the GITT curve): pristine β-V_2O_5—black, $Na_{0.4}V_2O_5$—red, $Na_{0.7}V_2O_5$—blue, NaV_2O_5—green.

During further discharge beyond Region II and until the end of the first discharge at 2.0 V, reflections corresponding to $Na_{0.7}V_2O_5$ decrease in intensity, while new reflections appear and increase in intensity (Region III in Figure 4a), evidencing another two-phase reaction from $Na_{0.7}V_2O_5$ to more sodium-rich $Na_xV_2O_5$ (phase region shown as green in GITT, Figure 1). The discontinuous variation is detected by the appearance of the new 100 reflection at 5.0°, while reflections from $Na_{0.7}V_2O_5$ decrease in intensity (Figures 3 and 4a). This two-phase transformation did not finish at the end of the first discharge at 2.0 V due to the nonequilibrium conditions in the *in situ* cell configuration.

The sodium-rich phase also has a monoclinic structure and can be indexed with space group $P2_1/m$. The Na content of this phase, formed at the end of the two-phase reaction (2.0 V), was estimated as NaV_2O_5 from GITT, with lattice parameters of a = 9.5437(1) Å, b = 3.6123(1) Å, c = 6.3546(1) Å, β = 88.26(1)°. A successful Rietveld structure refinement could not be achieved for NaV_2O_5, due to the low intensity of the reflections corresponding to this phase in the SXRD pattern (Figure 4a) and the overlapping of these reflections with those corresponding to the majority phase $Na_{0.7}V_2O_5$. However, a reliable structural model of NaV_2O_5 was proposed based on the refined lattice parameters from SXRD data under *operando* conditions (pattern no. 145, see refinement in Figure S1d), which was later confirmed by HRTEM results, discussed below. Remarkably, the significant shift of 100 to lower angles during this two-phase transition involves a further widening of the interlayer spacing from 8.5 Å in $Na_{0.7}V_2O_5$ to 9.5 Å in NaV_2O_5 to allow further Na^+ ion uptake (Figure 4b and Table 1).

The evolution of structural parameters is displayed in Figure 4b. At the beginning of the first discharge, the phase β-V_2O_5 ($P2_1/m$) accommodates Na-ions via a two-phase mechanism up to a limiting stoichiometry of $Na_{0.4}V_2O_5$ ($C2/m$) accompanied by an increase of lattice parameter a. The change from P to C centering of the unit cell results from the slab-gliding of the V_2O_5 layers by $b/2$ along b. After that, sodium uptake goes through a solid-solution mechanism up to $Na_{0.7}V_2O_5$ ($C2/m$), through which a gradually decreases. Ultimately, further sodium uptake with formation of sodium-rich NaV_2O_5 ($P2_1/m$) occurs via a two-phase reaction accompanied by further increase of lattice parameter a. As before, the change from C to P centering of the unit cell arises from the $b/2$ slab-gliding of the V_2O_5 layers along the b axis; however, in this case, the displacement occurs in the opposite direction.

The evolution of the lattice parameters of the unit cell (Figure 4b) and the overall diffraction profile (Figure 4a) observed during discharge of the *in situ* cell are reproduced during the charge process, demonstrating the reversibility of both structural changes and sodium intercalation in β-V_2O_5. This is nicely portrayed in the waterfall plot of synchrotron diffraction patterns shown in Figure S2, where the structural evolution upon charge mirrors that observed during discharge, returning to a fully charged phase with structural parameters matching those of pristine β-V_2O_5 (Figure 4b and Table 1).

Based on the structural predictions from fitting of *operando* synchrotron diffraction patterns, transmission electron microscopy (HRTEM) micrographs with their respective Fourier transforms can be indexed in the zone axis [001] for pristine β-V_2O_5, S.G. $P2_1/m$ (Figure 5a); electrochemically synthesized $Na_{0.5}V_2O_5$, S.G. $C2/m$ (Figure 5b); and electrochemically synthesized NaV_2O_5, S.G. $P2_1/m$ (Figure 5c). β-V_2O_5 exhibits the characteristic 7.1 Å interlayer distance and its Fourier transform is in good agreement with the reciprocal space of $P2_1/m$ space group (Figures 5a and S3a). The electron micrograph of a crystal of $Na_{0.5}V_2O_5$ in Figure 5b exhibits a d-spacing of ~8.5 Å throughout the entire area shown. The crystal orientation can be identified with the reciprocal lattice of a C-type cell, where ~8.5 Å is half of the a lattice parameter, compatible with the $C2/m$ symmetry (Figures 5b and S3b). The high-resolution micrograph in Figure 5c corresponds to a crystal of NaV_2O_5 oriented along the [001] zone axis according to the periodicity of ~9.5 Å, *i.e.* the d-spacing, that runs along the whole area, with perpendicular planes spaced at ~3.5 Å.

https://doi.org/10.1021/acs.chemmater.5c01520
Chem. Mater. 2025, 37, 8649−8663

The Fourier transform shows diffraction maxima according to this metric. All diffraction maxima can be assigned to a primitive cell in [001] projection. Likewise, image contrasts in Figure S3c and the corresponding Fourier transform can be interpreted on the basis of a primitive cell, now in the [111] projection. In summary, these results indicate that the NaV_2O_5 phase presents a primitive cell whose reciprocal lattice is compatible with the $P2_1/m$ symmetry space group, and an interlayer distance of ~9.5 Å.

The structures of all $Na_xV_2O_5$ phases developed during discharge−charge cycling are depicted in Figure 6. Our

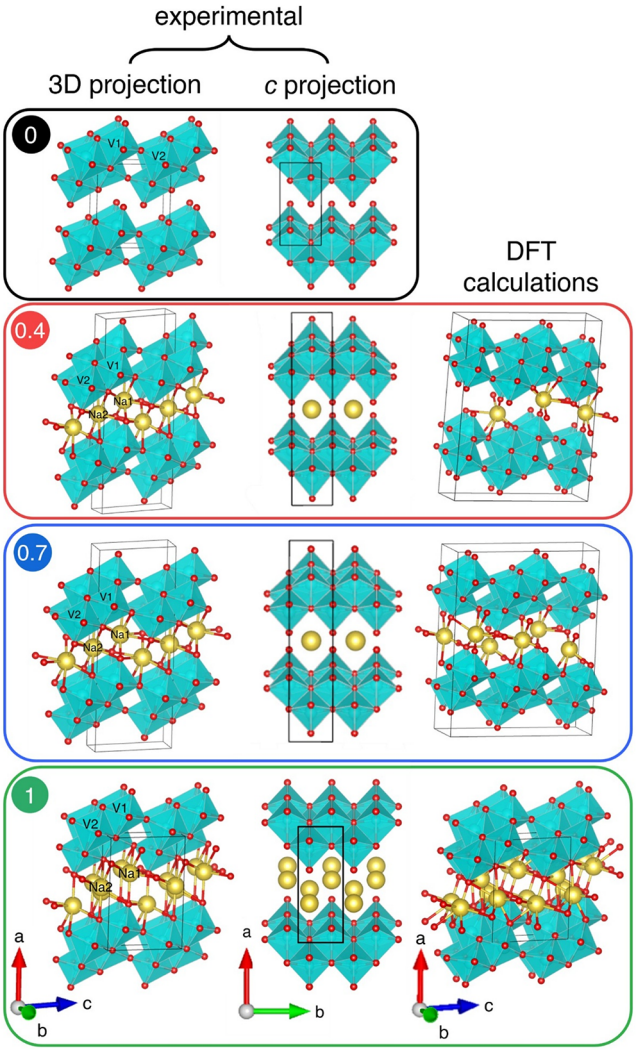

Figure 6. Structural models of the β-$Na_xV_2O_5$ system obtained through experimental methods (SXRD and HRTEM) and DFT(PBE + U) + D3-optimized calculations. Unit cells are shown. VO_6 octahedra—turquoise, oxygen—red, sodium—yellow.

findings unveil a fully reversible phase transition sequence during Na intercalation, $P2_1/m \rightarrow C2/m \rightarrow P2_1/m$, and the adaptability of such layered structure driven by the facile slab gliding of V_2O_5 layers along the crystallographic b direction to accommodate varying amounts of Na ions. The structures of pristine β-V_2O_5 and $Na_xV_2O_5$ phases are made of distorted VO_6 bioctahedra arranged in chains sharing edges, connected to the adjacent chains through the bioctahedra corners, leading to layers stacked along the a-axis, the difference being the relative position of the layers with respect to each other. Sodium positions in $Na_xV_2O_5$ were determined using the BVS-DM analysis (see details in the Supporting Information). In $Na_xV_2O_5$, sodium ions occupy two positions, Na1 and Na2, in the interlayer space (Figure S4). In the $Na_{0.4}V_2O_5$−$Na_{0.7}V_2O_5$ composition range, both Na1 and Na2 are eight-coordinated forming distorted NaO_8 prisms (Figure S4); whereas in NaV_2O_5, intercalated Na^+ ions are seven-coordinated (Na1) and six-coordinated (Na2), forming respective NaO_7 capped octahedra and NaO_6 trigonal prisms (Figure S4). Main crystallographic parameters of structural Rietveld refinements of $Na_{0.4}V_2O_5$ and $Na_{0.7}V_2O_5$ are given in Table S2, while the atomic coordinates of the proposed structure model of NaV_2O_5 are shown in Table S3. As expected, the occupancy of both Na1 and Na2 increases from 0.27(1) and 0.26(1) in $Na_{0.4}V_2O_5$, to 0.66(1) and 0.37(1) in $Na_{0.7}V_2O_5$, respectively. However, the increase in occupancy is more pronounced for Na1 than for Na2. This is explained by the longer Na1−Na1 interionic distances, which minimize electrostatic repulsions, compared to the Na1−Na2 distances (Table S4). It is important to note that once these calculated occupancy values are converted to the number of sodium ions per formula unit, they align closely with the nominal compositions: x = 0.43 for $Na_{0.4}V_2O_5$ and x = 0.70 for $Na_{0.7}V_2O_5$. Considering this, the slab-gliding observed during the $P2_1/m \rightarrow C2/m \rightarrow P2_1/m$ phase transition can be rationalized. The initial β-V_2O_5 structure (S.G. $P2_1/m$) lacks both sufficient vacancies and an appropriate coordination environment to accommodate large ions such as Na^+ —unlike smaller cations like Li^+. As a result, upon the initial intercalation of sodium, a biphasic transition occurs, leading to the formation of the intermediate $Na_{0.4-0.7}V_2O_5$ phase with space group $C2/m$. This structural transformation involves slab-gliding along the b-axis, which increases the interlayer spacing. The expanded layers not only provide enough room to host the larger Na^+ ions but also afford a more favorable coordination environment. However, as the sodium content approaches x = 0.7, increasing Na^+−Na^+ interionic repulsion prevents further intercalation within the $C2/m$ framework with the given arrangement of sodium ions. To accommodate a higher sodium content (x > 0.7 Na^+/f.u.), some rearrangement of the V−O layers is needed, reverting to the original $P2_1/m$ symmetry. In this sodium-rich phase, two distinct Na sites (Na1 and Na2, see Figure 6) are present, each offering suitable coordination environments and reduced interionic repulsion. This rearrangement enables further sodium intercalation, up to a maximum of 1 Na^+/f.u.

DFT calculations were performed to confirm the structures obtained by experimental techniques. We have adopted the modeling procedure of different $Na_xV_2O_5$ phases for DFT calculations from our previous study.[26] All supercells represented by these phases were created by doubling the initial β-V_2O_5 bulk unit cell with $P2_1/m$ space group in the b-, c-directions (112 atoms) and further insertion of Na atoms in a random way to obtain $Na_xV_2O_5$ formulas as close as possible to those studied experimentally. Finally, each supercell was optimized in terms of both the cell shape and internal atomic coordinates using variable-cell calculations. The whole procedure was repeated a few times, always using all parameters obtained from the previous run to get better convergence. In the present paper, starting from the previously optimized $Na_{0.375}V_2O_5$ system (equivalent to the experimental $Na_{0.4}V_2O_5$ phase),[26] we further increased the number of Na ions in the supercell (11 atoms) in random positions to get the $Na_{0.6875}V_2O_5$ phase, which corresponds to the experimental

https://doi.org/10.1021/acs.chemmater.5c01520
Chem. Mater. 2025, 37, 8649−8663

$Na_{0.7}V_2O_5$ phase (Figure 4). After optimization of the supercell, the equilibrium lattice constants were found to be a = 16.617 Å, b = 3.628 Å, c = 6.444 Å and α = 90.0°, β = 88.3°, γ = 89.6°. The optimized lattice constants are in very good agreement with the experimental data (Table S5). The deviation of a and b is less than 0.5%, whereas that of c is less than 2% relative to the refinement results. Importantly, our DFT calculations properly reflect the experimentally observed shortening of the a parameter with increasing sodium content (Table S5): 17.1623(8) Å for x = 0.4 and 16.6951(6) Å for x = 0.7, illustrating that the obtained crystal structure information is reliable. Further loading of sodium led to the hypothetical $Na_2V_2O_5$ phase (considering full occupancy of both sodium sites), which corresponds to the experimental NaV_2O_5 composition with partial occupancy of sodium sites. The resulting increase, however, of the interlayer spacing to 8.522 Å, is lower than the experimental value (Table S5), even if the initial structure for geometry optimization was the experimentally obtained configuration with S.G. $P2_1/m$. However, other lattice parameters, namely c = 6.396 Å and β = 86.97°, barely exhibit any deviation from the experimental values (Table S5). The observed discrepancy in the a-parameter relative to experimental results could be attributed to solvent cointercalation, a process previously reported in layered cathode materials for both Li-ion and Na-ion batteries when PC —as used in this study— or diglyme are employed as electrolyte solvents.[47−49] In the present case, cointercalation is most likely occurring during the slab-gliding associated with the $C2/m \rightarrow P2_1/m$ transition, specifically in the transformation from $Na_{0.7}V_2O_5$ to NaV_2O_5. This structural rearrangement creates additional interlayer space, which may facilitate the incorporation of solvent molecules alongside sodium ions. To better understand this discrepancy, our group is currently undertaking a comprehensive investigation of the NaV_2O_5 phase, combining experimental techniques with first-principles simulations to elucidate the role and impact of cointercalation in this system.

Table 2 compares the V−O bond lengths in the sodiated $Na_xV_2O_5$ phases determined experimentally. The bond distances for $Na_{0.4}V_2O_5$ and $Na_{0.7}V_2O_5$ were obtained through Rietveld refinement using *operando* SXRD data. In contrast, the bond lengths for fully sodiated NaV_2O_5 were derived from the structural model proposed on the basis of *operando* SXRD and HRTEM analysis. Among the two vanadium−oxygen octahedra, V1−O units are less sensitive to structural changes than V2−O octahedra. Upon the transformation from β-V_2O_5 to $Na_{0.4}V_2O_5$, an overall increase in V−O bond lengths is observed, primarily attributed to the decrease in vanadium oxidation state, which leads to an increase in the vanadium ionic radius. However, during the subsequent formation of $Na_{0.7}V_2O_5$, a shortening of V2−O bond distances is noted. This counterintuitive contraction likely results from a structural rearrangement of the layers that reduces the a lattice parameter (Table 1). The increase in V−O bond lengths upon transformation into NaV_2O_5 reflects the continued reduction of vanadium and the associated increase in its ionic radius. The distortion parameters (*i.e.*, bond length distortion index and bond angle variance) were determined on the basis of the expressions introduced by Baur[50] and Robinson et al.,[51] respectively. Notably, sodium intercalation also induces a progressive decrease in octahedral distortion, as indicated by both the bond length distortion index and the bond angle variance. This trend toward increased local symmetry is consistent with observations from *operando* XAS, which will be discussed in the following section.

Table 2. Bond Lengths of β-$Na_xV_2O_5$ System as Deduced from SXRD Data

bond length/Å	β-V_2O_5	$Na_{0.4}V_2O_5$	$Na_{0.7}V_2O_5$	NaV_2O_5[a]
V1−O1	2.032(4)	2.343(3)	2.234(6)	2.284
V1−O1′ (x2)	1.859(9)	1.827(4)	1.851(4)	1.8223
V1−O3	1.676(7)	1.798(7)	1.805(7)	1.932
V1−O4	1.662(6)	1.562(5)	1.681(5)	1.810
V1−O5	2.099(5)	2.140(4)	2.097(8)	1.980
average bond length/Å	1.909	1.916	1.920	1.9421
bond length distortion index	0.115	0.113	0.085	0.080
bond angle variance/deg^2	133.9	78.65	72.59	45.63
V2−O1	2.228(4)	2.492(2)	2.073(8)	2.208
V2−O2	1.609(4)	1.895(8)	1.808(7)	1.816
V2−O3	1.944(5)	1.916(2)	1.913(5)	2.017
V2−O4	2.050(6)	2.105(6)	2.139(6)	2.201
V2−O5 (x2)	1.879(2)	1.851(6)	1.830(4)	1.8310
average bond length/Å	1.947	2.019	1.932	1.9839
bond length distortion index	0.087	0.093	0.060	0.065
bond angle variance/deg^2	89.18	90.74	26.47	29.05

[a]Bond lengths of the proposed model of NaV_2O_5 phase according to operando SXRD and HRTEM data.

3.3. X-ray Spectroscopy Study. Changes in the local structure and electronic environment of vanadium atoms during a full discharge/charge cycle were analyzed through *operando* XAS measurements in the vanadium K-edge energy range. Figure 7a,b show the X-ray absorption near-edge structure (XANES) region of the collected spectra. The first collected spectrum (x = 0) and β-V_2O_5 reference show very similar pre-edge signal and absorption edge energies, confirming V^{5+} as the oxidation state of vanadium at the very beginning of discharge. The pre-edge signal corresponds to electronic transitions between V 1*s* and hybrid V 3*d*−O 2*p* states,[52,53] evidencing a loss of centrosymmetry of the vanadium site.

Both pre-edge signal and absorption edge energies progressively shift to lower values upon discharge (black arrows in Figure 7a,b), pointing to the reduction of V^{5+} to V^{4+}, caused by sodium intercalation into β-V_2O_5.[54] In addition, the discharge process causes the intensity of the pre-edge signal to decrease, suggesting changes in the first shell of vanadium (*i.e.*, VO_6 octahedra) toward more symmetric configurations.[52,55] Besides, two isosbestic points can be observed at the pre-edge signal and the near-edge regions (red arrows in Figure 7a,b), which reveal phase transformations occurring during the discharge process, as concluded from *operando* synchrotron diffraction. On the other hand, during the charge process, both pre-edge signal and edge positions shift back to higher energy values upon sodium extraction, showing a similar behavior but in the opposite direction to that observed during the discharge process. In addition, the last spectrum in charge greatly resembles the first spectrum in discharge (purple and black spectra in Figure 7b and 7a, respectively), in agreement with the reversibility of sodium (de)intercalation in β-V_2O_5, observed in *operando* diffraction. XAS results are also in good agreement with the galvanostatic electrochemical profile (Figure 1), demonstrating complete extraction of intercalated sodium from NaV_2O_5 with formation of β-V_2O_5.

https://doi.org/10.1021/acs.chemmater.5c01520
Chem. Mater. 2025, 37, 8649−8663

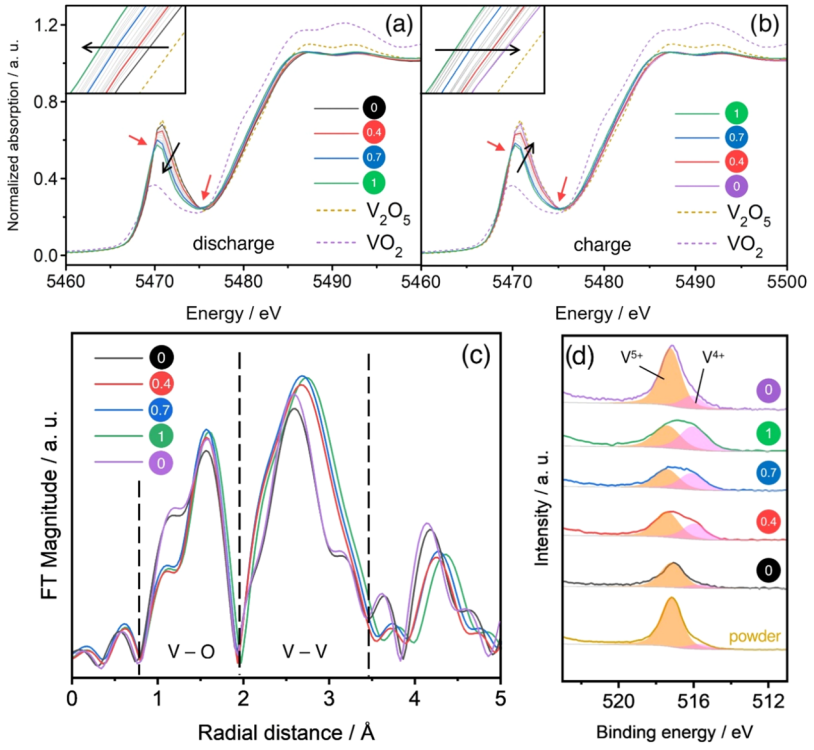

Figure 7. (a, b) XANES spectra at the V K-edge collected during discharge (a) and charge (b) processes corresponding to the (de)intercalation of 1 Na^+. Black arrows: shift of the spectra; red arrows: isosbestic points. The inset depicts a closer view of the edge region. *Ex situ* spectra of VO_2 and β-V_2O_5 powder are included, as references for V^{4+} and V^{5+}, respectively; (c) Fourier transform curves of the FT-EXAFS spectra (k^3 - weighted) at the V K-edge of the β-$Na_xV_2O_5$ system; (d) Selected region of XPS spectra (V $2p_{3/2}$ signal) of *ex situ* electrodes corresponding to β-V_2O_5 and $Na_xV_2O_5$ phases. The spectrum of β-V_2O_5 powder is included as a reference. V^{5+} and V^{4+} signals are labeled.

The phase-corrected Fourier Transform Extended X-ray Absorption Fine Structure (FT-EXAFS) region (energy range: 5485−5700 eV) of the XAS spectra (Figure 7c) provides more information about the local structure of the first shell (V−O octahedra) and the second shell (V−V bonds) of the environment of the central atom, vanadium. Considering the change in the FT-EXAFS curve upon sodiation, the sodium intercalation entails changes in the local structure of the vanadium atoms, confirming the observed structural changes during the phase transformations. The signal showing two components between 0.8 and 2.0 Å corresponds to the first shell of atoms, that is, the VO_6 octahedra of the layered structure. The length of these V−O bonds increase slightly during the phase transformation of the pristine β-V_2O_5 into $Na_{0.4}V_2O_5$, as evidenced by the decrease in the shorter-length component, the increase in the longer-length component, and the slight shift of the second component toward higher distances. Another slight shift of the longer V−O component indicates an extension of bond lengths upon transformation into $Na_{0.7}V_2O_5$, which is also observed for the subsequent transition into NaV_2O_5. This evolution of the V−O bond distances closely aligns with the trend of the values obtained from SXRD refinement data (Table 2), evidencing the phase transformations upon (de)sodiation. On the other hand, the shift toward higher distances of the signal corresponding to the second shell (*i.e.*, V−V bonds) centered at ∼2.6 Å indicates a slight expansion of the layers within the *bc* crystallographic plane, which is consistent with the SXRD results shown in Table 1. In addition, it is important to note the reversibility of the local structure, as indicated by the similarity of the pristine and the fully charged β-V_2O_5 spectra.

Ex situ XPS experiments, performed on discharged electrodes with different amounts of intercalated sodium (Figure 7d), confirm the conclusions deduced from XAS results. This *ex situ* procedure allowed to "mimic" the *operando* conditions from XAS experiments and to analyze the samples under equilibrium conditions. The selected region of the spectra shows the signal from V $2p_{3/2}$ (520−515 eV).[56] The survey spectrum can be found in Figure S5. V^{5+} contribution to the V $2p_{3/2}$ signal decreases upon sodium intercalation, while V^{4+} contribution gains intensity: for the pristine β-V_2O_5 electrode, V^{5+} contribution is totally dominant, while at the end of the discharge, for $x = 1$, V^{5+} and V^{4+} coexist showing a very similar abundance. A slight V^{4+} contribution is observed in both pristine samples (powder and electrode), which may be due to impurities on the surface of the samples or electrode processing. In any case, the oxidation state of vanadium for both β-V_2O_5 powder and electrode is very similar. After fully charging, both contributions come back to a state similar to that exhibited by the pristine electrode. Table 3 shows the numerical results of the contributions, provided by spectra fitting. Note the concordance between the formal oxidation state of vanadium obtained experimentally (only considering the V^{4+} formed upon redox reaction, *i.e.* excluding preexisting V^{4+} before discharge) and the calculated value based on the nominal amount of intercalated sodium. From these results, it can be deduced that vanadium undergoes a reduction from V^{5+} to V^{4+} upon sodium intercalation, reaching a formal oxidation state of 4.5+ when discharging the cell down to 2 V, corresponding to the intercalation of 1 Na^+. When the cell is fully charged, the oxidation state of vanadium returns to V^{5+},

https://doi.org/10.1021/acs.chemmater.5c01520
Chem. Mater. 2025, 37, 8649−8663

Table 3. Fitted Contributions of the XPS Signal from V $2p_{3/2}$ of β-V_2O_5 Powder and *Ex Situ* Electrodes Bearing β-V_2O_5 and Selected $Na_xV_2O_5$ Compositions

signal	V^{5+}/ %	V^{4+}/ %	formal oxidation state of vanadium	corrected oxidation state of vanadium[a]	nominal oxidation state of vanadium
β-V_2O_5 (powder)	90.8	9.2	+4.908	+5	+5
β-V_2O_5 (electrode)	90.9	9.1	+4.909	+5	+5
$Na_{0.4}V_2O_5$	70.9	29.1	+4.709	+4.780	+4.8
$Na_{0.7}V_2O_5$	53.4	46.6	+4.534	+4.587	+4.65
NaV_2O_5	49.0	51.0	+4.490	+4.539	+4.5
charged β-V_2O_5	90.5	9.5	+4.905	+4.996	+5

[a]considering exclusively V^{4+} formed upon redox reaction.

resembling that of pristine β-V_2O_5, thereby highlighting the reversible nature of sodium (de)intercalation.

3.4. Impedance and Kinetic Study. PEIS experiments were conducted to investigate the electrical resistance opposed to the charge transport during sodium (de)intercalation. Figure 8 shows the Nyquist plots of pristine β-V_2O_5, the sodiated

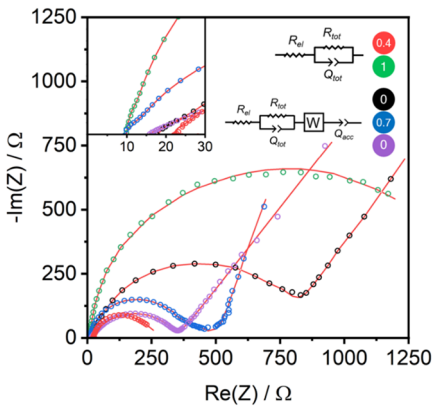

Figure 8. Nyquist plots of β-V_2O_5 and selected $Na_xV_2O_5$ compositions. Data fitting is depicted as a red line. Equivalent electrical circuits employed for data fitting are included.

$Na_xV_2O_5$ phases and charged β-V_2O_5. Note that these measurements were performed using a three-electrode cell, which allows the contribution from the working electrode without any interference from the sodium anode to be investigated. All the PEIS experiments were carried out on the same cell at the corresponding potential to reach the selected composition: OCV for pristine β-V_2O_5, 3.1 V for $Na_{0.4}V_2O_5$, 2.75 V for $Na_{0.7}V_2O_5$, 2 V for NaV_2O_5 and 3.6 V for the charged β-V_2O_5.

Figure 8 includes the equivalent circuits employed for data fitting in each phase. For pristine β-V_2O_5, $Na_{0.7}V_2O_5$ and charged β-V_2O_5, a modified Randles circuit,[57] including an additional constant phase element (CPE) in series has been employed. This modified Randles circuit has been widely proposed by previous authors to fit similar spectra.[58,59] On the other hand, for $Na_{0.4}V_2O_5$ and NaV_2O_5 phases, the Warburg element and the extra CPE were not needed in the equivalent circuit to fit the recorded impedance response.

The physicochemical processes occurring in the electrochemical cell are modeled by the elements of the equivalent circuit, based on their respective impedance response. For instance, the resistance opposed to the migration of solvated Na^+ ions through the electrolyte (the fastest process taking place in the cell) as well as the ohmic resistances coming from the separator, cable connections, etc. are modeled by a resistor, R_{el}. This resistance is calculated from the x-intercept at the high-frequency range (1 MHz−0.1 MHz) as it is graphically shown in the inset of Figure 8.

The following element, an RCPE (resistor with a resistance R_{tot} in parallel with CPE with a psudocapacitance Q_{tot}) is characterized by the depleted semicircle depicted in the Nyquist plots at medium frequency values (10−1 Hz), which involves a constant phase element instead of a pure capacitor. CPEs are generally used for modeling the impedance response of an electrochemical cell following a nonideal behavior caused by irregularities on the surface of the electrode (nonuniformity, roughness, defects...) and on its interface with the electrolyte.[60] The resistor R_{tot} comprehends the resistance related to the charge transfer (CT) process as well as the resistance opposed to the Na^+ ions penetration through the insulating cathode-electrolyte interface (CEI). On the other hand, the CPE Q_{tot} describes the pseudocapacitance related to the CEI layer as well as to the double electrical layer in the interface of the positive electrode and the electrolyte, induced by the presence of Na^+ ions. Note that the Nyquist plots could depict two differentiated semicircles, ascribed to two different RCPE pairs, one corresponding to the CEI layer and the other describing the charge transfer/double layer phenomena. However, this is not the case as probably their relaxation frequencies are not different enough and hence, only R_{tot} and Q_{tot} could be determined.

In the low-frequency range (100−10 mHz), where the slowest processes take place, impedance data from pristine β-V_2O_5, $Na_{0.7}V_2O_5$ and charged β-V_2O_5 show a spike (that is, a linear relation between $-\mathrm{Im}(Z)$ and $\mathrm{Re}(Z)$) immediately after the semicircle, whereas $Na_{0.4}V_2O_5$ and NaV_2O_5 phases do not exhibit this feature at low frequency. In the samples exhibiting a spike in their Nyquist plots at low-frequency values, the narrow region of this spike with a 45° slope is modeled by a Warburg element in the equivalent circuit, which is ascribed to the semi-infinite diffusion of Na^+ ions within the region near the surface of the particles of the positive electrode. Following this narrow region, a deviation from the 45° slope toward higher angles is observed. Such behavior is described by the extra CPE in series, whose pseudocapacitance Q_{acc} accounts for the accumulation of Na^+ ions on the surface of the positive electrode, caused by the limited sodium diffusion kinetics or by reaching open circuit conditions.[59,61] The Nyquist plots of $Na_{0.4}V_2O_5$ and NaV_2O_5 do not exhibit the characteristic low-frequency spike typically associated with sodium-ion diffusion, attributed to the high dispersion in the impedance response at low frequencies, which prevented the acquisition of reliable data in this region, despite using the same electrochemical cell, frequency range and potential holding time.

Table S6 displays the results of the spectra fitting. After a decrease in the total resistance R_{tot} upon the phase transformation from β-V_2O_5 into $Na_{0.4}V_2O_5$,[26] R_{tot} increases upon sodium intercalation. Since the different contributions of CEI and CT resistances to R_{tot} are not resolved, it is not possible to determine whether this increase is due to one or the other resistance. However, it is expected that the CT resistance, which may change due to the newly formed phase with a different structure and composition, will contribute more to

https://doi.org/10.1021/acs.chemmater.5c01520
Chem. Mater. 2025, 37, 8649−8663

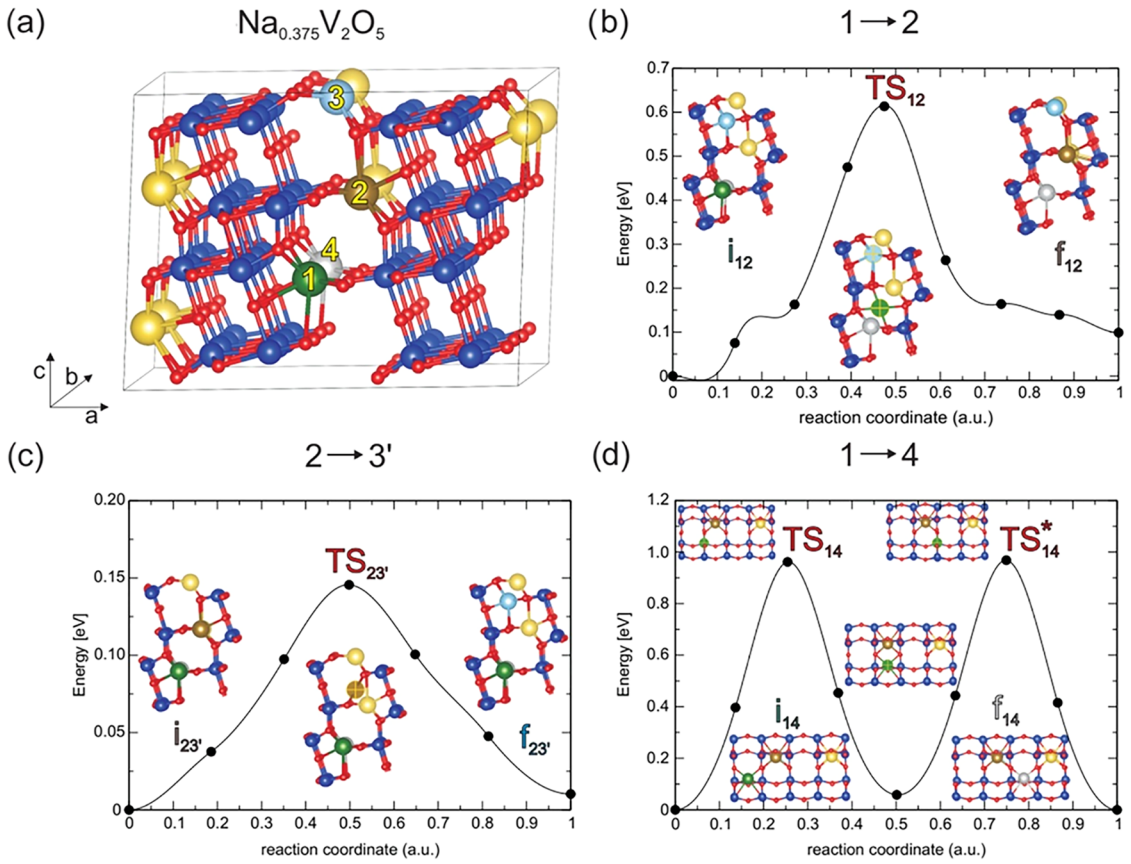

Figure 9. (a) Na atoms in different colors and labeled with numbers in the supercell representing the $Na_{0.375}V_2O_5$ phase; (b–d) Three minimum energy CI-NEB paths for the Na migration. The minimum energy is set to zero. The Na, V and O atoms are shown as yellow, blue and red spheres, respectively. The movable atom is labeled by a cross, for transparency.

the total resistance. Interestingly, the charged β-V_2O_5 exhibits a lower R_{tot} compared to the pristine compound, suggesting that the charge transfer is less impeded after CEI formation.

The sodium diffusion coefficient D_{Na+} was determined using PEIS and PITT techniques (see details in the Supporting Information). In both cases, the calculation is based on the data corresponding to the region where semi-infinite diffusion conditions are fulfilled, that is (a) in PEIS experiments, the frequency region where the spike exhibited by the impedance data in the Nyquist plots depicts a 45° slope; and (b) in PITT experiments, the time range where the current vs time relaxation follows the Cottrell law, *i.e.* where I is proportional to $1/\sqrt{t}$. Parameters related to the semi-infinite diffusion conditions, *i.e.* A_W for PEIS and $I\sqrt{t}$ for PITT, were deduced from the values of the minimum of $-\mathrm{Im}(Z)^*\omega^{1/2}$ vs ω plot (Figure S7) and the maximum of the $(I\sqrt{t})^2$ vs t plot (Figure S8), respectively.[62] Table S7 shows the parameters required for calculating D_{Na+}, as well as the resulting D_{Na+}. Overall, the D_{Na+} across the entire β-$Na_xV_2O_5$ system remains high and relatively constant, with only a slight increase that may be associated with the expansion of the a lattice parameter.

The migration of sodium cations was examined by CI-NEB for the previously optimized $Na_{0.375}V_2O_5$ system.[26] In this study, we consider two migration paths of Na ions along the crystallographic c direction (1 → 2, 2 → 3′) and one along the b direction (1 → 4) (Figure 9). In each case, we doubled the supercell representing the $Na_{0.375}V_2O_5$ phase in the b direction, then removed one Na atom to obtain the initial (i_{path}) and final (f_{path}) state of the given path, and finally both structures were optimized. The diffusion barrier (TS) is reported with respect to the total energy of the initial structure that is set to 0 eV. For some systems with the removed Na, the additional reorganization of atoms appears after geometry optimization. As a result, the initial and/or final configuration of the path can be slightly different from those initially defined for the $Na_{0.375}V_2O_5$ configuration presented in Figure 9a. This is the case for the 2 → 3′ path (Figure 9c), where after optimization of the final structure, the Na atom from position 3 (position Na2 in β-V_2O_5, see Figure 6) moved spontaneously to the position denoted as 3′ (position Na1 in β-V_2O_5, see Figure 6). After that, the total energy is almost the same (higher by 0.01 eV). Thus, the 2 → 3′ path shows the jump from one Na1 position to another. The smooth character of the calculated minimum energy path presented in Figure 9c implies a simple process with a very low energy barrier of 0.15 eV. Therefore, the Na1 positions in the $Na_xV_2O_5$ bulk should easily accept and release Na ions to decrease their electrostatic interactions in the channels. Contrary to the 2 → 3′ path, where a Na ion jumps between two neighboring Na1 sites along the c direction, the 1 → 4 path (Figure 9d) corresponds to such migration along the b direction between two sites separated by $2b$ periods of the β-V_2O_5 lattice. In this case, two equivalent transition states (TS_{14}, TS^*_{14}) exist on the path, since the atomic environment of Na ion in both positions 1 and 4 is also the same. Notably, the diffusion barrier of Na along the b direction (0.96 eV) is much larger than that along the c direction (0.15 eV). Comparison of the coordination sphere of the Na atom at TS_{14}(TS^*_{14}) and $TS_{23'}$ reveals that, in both

https://doi.org/10.1021/acs.chemmater.5c01520
Chem. Mater. 2025, 37, 8649−8663

cases, it exhibits a distorted square-planar geometry with four Na−O bonds of 2.00−2.25 Å in the first case, and of 2.30−2.34 Å in the second case. Hence, the much weaker interaction between Na and the adjacent O atoms in the latter case leads to its easy overcome of the energetic barrier along the *c* direction. Finally, we analyze the 1 → 2 path (Figure 9b) that can be roughly considered as a superposition of 2 → 3′ and 1 → 4 paths. Here, the Na atom from one Na1 site (1) migrates to another Na1 site (2) that is moved by one period in the *b* direction and around three-quarters period in the *c* direction. Furthermore, this migration is connected with simultaneous jump of the second Na atom from position 3′ to 3. Taking into account that this second process should have very low energetic barrier (~0.15 eV), the first one with the TS_{12} of 0.62 eV thus determines the diffusion step. On the 1 → 2 path (nine images), the first three images correspond to the jump from the Na1 site to Na2 one (~0.14 eV) along the *c* direction, the next three to overcome an energetic barrier (TS_{12}) from one Na2 site to another along the *b* direction and the last three to the jump from the Na2 site to Na1 one along the *c* direction. The sodium atom in the TS_{12} also exhibits a distorted square-planar geometry with all Na−O distances of 2.18−2.2 Å slightly longer than those in TS_{14}(TS^*_{14}), which explains the lower value of the transition state (by 0.34 eV).

4. CONCLUSION

In summary, we have thoroughly investigated the sodium intercalation mechanism in β-V_2O_5 using a combination of *operando* synchrotron diffraction and *operando* XAS and *ex situ* XPS. Sodium intercalation in β-V_2O_5 induces a series of reversible phase transitions, driven by slab-gliding of the V−O bioctahedra layers, while preserving their structural building blocks. The following $Na_xV_2O_5$ phases and corresponding crystallographic symmetries were identified with increasing sodium content: $x = 0$ ($P2_1/m$), $x = 0.4$−0.7 ($C2/m$), and $x = 1$ ($P2_1/m$). The reversibility of these transitions was corroborated by *operando* XAS. The progressive expansion of the interlayer spacing —7.1 Å in pristine β-V_2O_5, 8.5 Å in $Na_{0.4}V_2O_5$−$Na_{0.7}V_2O_5$, and 9.5 Å in fully sodiated NaV_2O_5— to accommodate increasing amounts of Na^+ ions was further confirmed by HRTEM. DFT calculations accurately reflect the experimentally observed increase in the *a* lattice parameter with increasing sodium content, illustrating how the evolving crystal structures accommodate additional sodium ions. In addition, we have elucidated the evolution of the vanadium oxidation state during sodium intercalation, confirming the reduction from V^{5+} to V^{4+}, as demonstrated by XPS and the XANES region of XAS spectra. Moreover, sodium intercalation induces modifications in the local structure of vanadium, *i.e.* in the VO_6 octahedra and the shell of V−V bonds, as revealed by the analysis of the FT-EXAFS region of XAS spectra. Beyond structural and electronic effects, sodium intercalation enhances reaction kinetics, by lowering the charge transfer resistance and improving Na^+ ion diffusivity (D_{Na+}) by an order of magnitude. Notably, migration paths calculations reveal that Na^+ ion diffusion is energetically favored along the *c* direction, while it is kinetically hindered along the *b* direction. *Operando* synchrotron diffraction and *operando* XAS have proven to be powerful tools to elucidate the structural and electrochemical mechanism of sodium uptake in β-V_2O_5. This should be a strong stimulus to fully uncover electrochemical storage mechanisms of other metal-ion technologies such as Li^+, K^+, Mg^{2+} or Ca^{2+}, in β-V_2O_5 and other V_2O_5 cathode materials.

■ ASSOCIATED CONTENT

Supporting Information

The Supporting Information is available free of charge at https://pubs.acs.org/doi/10.1021/acs.chemmater.5c01520.

Additional HRTEM micrographs, *operando* SXRD refinements of the β-$Na_xV_2O_5$ system, waterfall plot of *operando* SXRD data during charge, survey XPS spectra of the β-$Na_xV_2O_5$ system, graphic determination of values required for D_{Na+} calculation, BVS-DM isosurfaces, Rietveld refinement results using *operando* and *ex situ* SXRD data from β-V_2O_5 and *operando* data from $Na_{0.4}V_2O_5$ and $Na_{0.7}V_2O_5$ phases, atomic coordinates of NaV_2O_5 proposed model, refined interionic distances of sodium in $Na_{0.4}V_2O_5$ and $Na_{0.7}V_2O_5$ phases (PDF)

Accession Codes

Deposition Numbers 2486719−2486720 contain the supplementary crystallographic data for this paper. These data can be obtained free of charge via the joint Cambridge Crystallographic Data Centre (CCDC) and Fachinformationszentrum Karlsruhe Access Structures service.

■ AUTHOR INFORMATION

Corresponding Author

Rafael Córdoba − *Departamento de Química y Bioquímica, Facultad de Farmacia, Universidad San Pablo-CEU, Madrid 28668, Spain;* orcid.org/0000-0003-3931-048X; Email: rafael.cordobarojano@ceu.es

Authors

Jakub Goclon − *Faculty of Chemistry, University of Bialystok, Bialystok 15-245, Poland;* orcid.org/0000-0002-4261-2799

Angelina Sarapulova − *Institute for Applied Materials (IAM), Karlsruhe Institute of Technology (KIT), Eggenstein-Leopoldshafen D-76344, Germany; Fraunhofer Institute for Solar Energy Systems, Department of Electrical Energy Storage, Freiburg 79110, Germany; Freiburg Materials Research Center (FMF), Freiburg 79104, Germany*

Julia Maibach − *Institute for Applied Materials (IAM), Karlsruhe Institute of Technology (KIT), Eggenstein-Leopoldshafen D-76344, Germany; Department of Physics, Chalmers University of Technology, Göteborg SE-412 96, Sweden;* orcid.org/0000-0003-1339-7804

Sonia Dsoke − *Institute for Applied Materials (IAM), Karlsruhe Institute of Technology (KIT), Eggenstein-Leopoldshafen D-76344, Germany; Fraunhofer Institute for Solar Energy Systems, Department of Electrical Energy Storage, Freiburg 79110, Germany; Freiburg Materials Research Center (FMF), Freiburg 79104, Germany*

Ester García-González − *Departamento de Química Inorgánica, Facultad de Ciencias Químicas, Universidad Complutense de Madrid, Madrid 28040, Spain;* orcid.org/0000-0002-5859-4070

François Fauth − *CELLS-ALBA Synchrotron, Barcelona 08290, Spain;* orcid.org/0000-0001-9465-3106

Alois Kuhn − *Departamento de Química y Bioquímica, Facultad de Farmacia, Universidad San Pablo-CEU, Madrid 28668, Spain;* orcid.org/0000-0002-4670-1473

Flaviano García-Alvarado − *Departamento de Química y Bioquímica, Facultad de Farmacia, Universidad San Pablo-CEU, Madrid 28668, Spain;* orcid.org/0000-0002-5698-2598

https://doi.org/10.1021/acs.chemmater.5c01520
Chem. Mater. 2025, 37, 8649−8663

Complete contact information is available at:
https://pubs.acs.org/10.1021/acs.chemmater.5c01520

Notes

The authors declare no competing financial interest.

■ ACKNOWLEDGMENTS

We thank MCIN/AEI/10.13039/501100011033/FEDER-UE for funding the projects PID2022-139039OB-C21 and PID2022-139039OB-C22; and AEI/10.13039/501100011033/Union Europea Next Generation EU/PRTR for funding the project TED2021-129427B−I00. A Financial support from Universidad San Pablo is also acknowledged. Rafael Córdoba wants to thank AEI and European Social fund/UE for the predoctoral grant BES-2017-080862. This work contributes to the research performed at the Center for Electrochemical Energy Storage Ulm-Karlsruhe (CELEST) and was partially funded by the Deutsche Forschungsgemeinschaft (DFG, German Research Foundation) under Germany's Excellence Strategy—EXC 2154—Project number 390874152 (POLiS Cluster of Excellence). We thank José Manuel Gallardo-Amores (High-pressure Laboratory, Universidad Complutense de Madrid) and María José Torralvo Fernández (Department of Inorganic Chemistry, Universidad Complutense de Madrid) for the synthesis of β-V_2O_5 and BET experiments, respectively. We thank the National Center for Electron Microscopy (CNME) at Universidad Complutense de Madrid, for support and access to instrumental facilities. The synchrotron diffraction experiments at ALBA were funded through a proposal with reference number 2018093055. We acknowledge DESY synchrotron, a member of the Helmholtz Association HGF, for the provision of experimental facilities. Parts of this research were carried out at PETRA III beamline P65. Beamtime was allocated for proposal(s) I-20200899. The *operando* XAS work was performed by using the Biologic potentiostat of PETRA-III beamline P02.1. We would like to thank Dr. Edmund Welter from Experiments Division at DESY for the technical support. This work was partly carried out with the support of the Karlsruhe Nano Micro Facility (KNMFi, www.knmf.kit.edu), a Helmholtz Research Infrastructure at Karlsruhe Institute of Technology (KIT, www.kit.edu). We gratefully acknowledge Polish high-performance computing infrastructure PLGrid (HPC Center: ACK Cyfronet AGH) for providing computer facilities and support within computational grant no. PLG/2022/015728.

■ REFERENCES

(1) Weckhuysen, B. M.; Keller, D. E. Chemistry, Spectroscopy and the Role of Supported Vanadium Oxides in Heterogeneous Catalysis. *Catal. Today* **2003**, *78* (1), 25−46.
(2) Chernova, N. A.; Roppolo, M.; Dillon, A. C.; Whittingham, M. S. Layered Vanadium and Molybdenum Oxides: Batteries and Electrochromics. *J. Mater. Chem.* **2009**, *19* (17), 2526−2552.
(3) Fu, Q.; Zhao, H.; Sarapulova, A.; Dsoke, S. V_2O_5 as a Versatile Electrode Material for Postlithium Energy Storage Systems. *Appl. Res.* **2023**, *2* (3), No. e202200070.
(4) Whittingham, M. S. Lithium Batteries and Cathode Materials. *Chem. Rev.* **2004**, *104* (10), 4271−4302.
(5) Murphy, D. W.; Christian, P. A.; DiSalvo, F. J.; Waszczak, J. V. Lithium Incorporation by Vanadium Pentoxide. *Inorg. Chem.* **1979**, *18* (10), 2800−2803.
(6) Tepavcevic, S.; Xiong, H.; Stamenkovic, V. R.; Zuo, X. B.; Balasubramanian, M.; Prakapenka, V. B.; Johnson, C. S.; Rajh, T. Nanostructured Bilayered Vanadium Oxide Electrodes for Rechargeable Sodium-Ion Batteries. *ACS Nano* **2012**, *6* (1), 530−538.
(7) Su, L. Y.; Winnick, J.; Kohl, P. Sodium Insertion into Vanadium Pentoxide in Methanesulfonyl Chloride-Aluminum Chloride Ionic Liquid. *J. Power Sources* **2001**, *101* (2), 226−230.
(8) Baddour-Hadjean, R.; Renard, M. S.; Pereira-Ramos, J. P. Enhanced Electrochemical Properties of Ball-Milled Gamma '-V_2O_5 as Cathode Material for Na-Ion Batteries: A Structural and Kinetic Investigation. *J. Power Sources* **2021**, *482*, No. 229017.
(9) García-Alvarado, F.; Tarascon, J. M.; Wilkens, B. Synthesis and Electrochemical Study of New Copper Vanadium Bronzes and of 2 New V_2O_5 Polymorphs - Beta'-V_2O_5 and Epsilon'-V_2O_5. *J. Electrochem. Soc.* **1992**, *139* (11), 3206−3214.
(10) García-Alvarado, F.; Tarascon, J. M. New Vanadium Bronzes $M_yV_2O_5$ (M = Cu or Ag; $0 < y < 0.85$): Structure and Lithium Intercalation. *Solid State Ion* **1993**, *63*−*65*, 401−406.
(11) Cocciantelli, J. M.; Gravereau, P.; Doumerc, J. P.; Pouchard, M.; Hagenmuller, P. On the Preparation and Characterization of a New Polymorph of V_2O_5. *J. Solid State Chem.* **1991**, *93* (2), 497−502.
(12) Safrany-Renard, M.; Emery, N.; Baddour-Hadjean, R.; Pereira-Ramos, J. P. γ'-V_2O_5: A New High Voltage Cathode Material for Sodium-Ion Battery. *Electrochim. Acta* **2017**, *252*, 4−11.
(13) Muller-Bouvet, D.; Baddour-Hadjean, R.; Tanabe, M.; Huynh, L. T. N.; Le, M. L. P.; Pereira-Ramos, J. P. Electrochemically Formed α'-NaV_2O_5: A New Sodium Intercalation Compound. *Electrochim. Acta* **2015**, *176*, 586−593.
(14) Baddour-Hadjean, R.; Renard, M. S.; Emery, N.; Huynh, L. T. N.; Le, M. L. P.; Pereira-Ramos, J. P. The Richness of V_2O_5 Polymorphs as Superior Cathode Materials for Sodium Insertion. *Electrochim. Acta* **2018**, *270*, 129−137.
(15) Filonenko, V. P.; Sundberg, M.; Werner, P.-E.; Zibrov, I. P. Structure of a High-Pressure Phase of Vanadium Pentoxide, β-V_2O_5. *Acta Crystallogr., Sect. B:Struct. Sci.* **2004**, *60* (4), 375−381.
(16) Leyzerovich, N. N.; Bramnik, K. G.; Buhrmester, T.; Ehrenberg, H.; Fuess, H. Electrochemical Intercalation of Lithium in Ternary Metal Molybdates $MMoO_4$ (M: Cu, Zn, Ni and Fe). *J. Power Sources* **2004**, *127* (1), 76−84.
(17) García-Moreno, O.; Alvarez-Vega, M.; García-Jaca, J.; Gallardo-Amores, J. M.; Sanjuán, M. L.; Amador, U. Influence of the Structure on the Electrochemical Performance of Lithium Transition Metal Phosphates as Cathodic Materials in Rechargeable Lithium Batteries: A New High-Pressure Form of $LiMPO_2$ (M = Fe and Ni). *Chem. Mater.* **2001**, *13* (5), 1570−1576.
(18) Pérez-Flores, J. C.; Villamor, R.; Ávila-Brande, D.; Amores, J. M. G.; Morán, E.; Kuhn, A.; García-Alvarado, F. VO_2F: A New Transition Metal Oxyfluoride with High Specific Capacity for Li Ion Batteries. *J. Mater. Chem. A* **2015**, *3* (41), 20508−20515.
(19) Arroyo-de Dompablo, M. E.; Gallardo-Amores, J. M.; Amador, U. Lithium Insertion in the High-Pressure Polymorph of $FePO_4$: Computational Predictions and Experimental Findings. *Electrochem Solid State Lett.* **2005**, *8* (11), No. A564.
(20) Arroyo-de Dompablo, M. E.; Amador, U.; Alvarez, M.; Gallardo, J. M.; García-Alvarado, F. Novel Olivine and Spinel $LiMAsO_4$ (M = 3d-Metal) as Positive Electrode Materials in Lithium Cells. *Solid State Ion* **2006**, *177* (26), 2625−2628.
(21) Padhi, A. K.; Archibald, W. B.; Nanjundaswamy, K. S.; Goodenough, J. B. Ambient and High-Pressure Structures of $LiMnVO_4$ and Its Mn^{3+}/Mn^{2+} Redox Energy. *J. Solid State Chem.* **1997**, *128* (2), 267−272.
(22) y de Dompablo, M. A.; Gallardo-Amores, J. M.; Amador, U.; Morán, E. Are High Pressure Materials Suitable for Electrochemical Applications? HP-V_2O_5 as a Novel Electrode Material for Li Batteries. *Electrochem. Commun.* **2007**, *9* (6), 1305−1310.
(23) Córdoba, R.; Kuhn, A.; Pérez-Flores, J. C.; Morán, E.; Gallardo-Amores, J. M.; García-Alvarado, F. Sodium Insertion in High Pressure β-V_2O_5: A New High Capacity Cathode Material for Sodium Ion Batteries. *J. Power Sources* **2019**, *422*, 42−48.
(24) Bhatia, A.; Pereira-Ramos, J.-P.; Arroyo-de Dompablo, M. E.; Baddour-Hadjean, R. An Exploratory Investigation of the High

Pressure β-V_2O_5 Polymorph as 3 V Cathode Material for Potassium-Ion Battery. *Electrochim. Acta* **2024**, *492*, No. 144311.
(25) Trócoli, R.; Parajuli, P.; Frontera, C.; Black, A. P.; Alexander, G. C. B.; Roy, I.; Arroyo-de Dompablo, M. E.; Klie, R. F.; Cabana, J.; Palacín, M. R. β-V_2O_5 as Magnesium Intercalation Cathode. *ACS Appl. Energy Mater.* **2022**, *5*, 11964−11969.
(26) Córdoba, R.; Goclon, J.; Sarapulova, A.; Fu, Q.; Maibach, J.; Dsoke, S.; Fauth, F.; Kuhn, A.; García-Alvarado, F. From High-pressure β-V_2O_5 to K-$Na_xV_2O_5$ (x = 0.4 − 0.55): A Structural, Chemical and Kinetic Insight into a Sodiated Phase with a Large Interlayer Space. *Appl. Res.* **2023**, *2*, No. e202200052.
(27) Herklotz, M.; Weiß, J.; Ahrens, E.; Yavuz, M.; Mereacre, L.; Kiziltas-Yavuz, N.; Dräger, C.; Ehrenberg, H.; Eckert, J.; Fauth, F.; Giebeler, L.; Knapp, M. A Novel High-Throughput Setup for in Situ Powder Diffraction on Coin Cell Batteries. *J. Appl. Crystallogr.* **2016**, *49* (1), 340−345.
(28) Fauth, F.; Peral, I.; Popescu, C.; Knapp, M. The New Material Science Powder Diffraction Beamline at ALBA Synchrotron. *Powder Diffr.* **2013**, *28* (S2), S360−S370.
(29) Rodríguez-Carvajal, J. Recent Advances in Magnetic Structure Determination by Neutron Powder Diffraction. *Phys. B Condens Matter* **1993**, *192* (1), 55−69.
(30) Momma, K.; Izumi, F. VESTA3 for Three-Dimensional Visualization of Crystal, Volumetric and Morphology Data. *J. Appl. Crystallogr.* **2011**, *44* (6), 1272−1276.
(31) Welter, E.; Chernikov, R.; Herrmann, M.; Nemausat, R. *A Beamline for Bulk Sample X-Ray Absorption Spectroscopy at the High Brilliance Storage Ring PETRA III*; Proceedings of the 13th International Conference on Synchrotron Radiation Instrumentation − SRI2018; AIP, 2019, 040002 .
(32) Ravel, B.; Newville, M. ATHENA, ARTEMIS, HEPHAESTUS: Data Analysis for X-Ray Absorption Spectroscopy Using IFEFFIT. *J. Synchrotron Radiat.* **2005**, *12* (4), 537−541.
(33) Parry, K. L.; Shard, A. G.; Short, R. D.; White, R. G.; Whittle, J. D.; Wright, A. ARXPS Characterisation of Plasma Polymerised Surface Chemical Gradients. *Surf. Interface Anal.* **2006**, *38* (11), 1497−1504.
(34) Giannozzi, P.; Baroni, S.; Bonini, N.; Calandra, M.; Car, R.; Cavazzoni, C.; Ceresoli, D.; Chiarotti, G. L.; Cococcioni, M.; Dabo, I.; Dal Corso, A.; de Gironcoli, S.; Fabris, S.; Fratesi, G.; Gebauer, R.; Gerstmann, U.; Gougoussis, C.; Kokalj, A.; Lazzeri, M.; Martin-Samos, L.; Marzari, N.; Mauri, F.; Mazzarello, R.; Paolini, S.; Pasquarello, A.; Paulatto, L.; Sbraccia, C.; Scandolo, S.; Sclauzero, G.; Seitsonen, A. P.; Smogunov, A.; Umari, P.; Wentzcovitch, R. M. QUANTUM ESPRESSO: A Modular and Open-Source Software Project for Quantum Simulations of Materials. *J. Phys.:Condens Matter* **2009**, *21* (39), No. 395502.
(35) Perdew, J. P.; Burke, K.; Ernzerhof, M. Generalized Gradient Approximation Made Simple. *Phys. Rev. Lett.* **1996**, *77* (18), No. 3865.
(36) Grimme, S.; Ehrlich, S.; Goerigk, L. Effect of the Damping Function in Dispersion Corrected Density Functional Theory. *J. Comput. Chem.* **2011**, *32* (7), 1456−1465.
(37) Vanderbilt, D. Soft Self-Consistent Pseudopotentials in a Generalized Eigenvalue Formalism. *Phys. Rev. B* **1990**, *41* (11), No. 7892.
(38) Dudarev, S. L.; Botton, G. A.; Savrasov, S. Y.; Humphreys, C. J.; Sutton, A. P. Electron-Energy-Loss Spectra and the Structural Stability of Nickel Oxide: An LSDA+U Study. *Phys. Rev. B* **1998**, *57* (3), No. 1505.
(39) Cococcioni, M.; de Gironcoli, S. Linear Response Approach to the Calculation of the Effective Interaction Parameters in the LDA+U Method. *Phys. Rev. B* **2005**, *71* (3), No. 35105.
(40) Monkhorst, H. J.; Pack, J. D. Special Points for Brillouin-Zone Integrations. *Phys. Rev. B* **1976**, *13* (12), No. 5188.
(41) Henkelman, G.; Jónsson, H. Improved Tangent Estimate in the Nudged Elastic Band Method for Finding Minimum Energy Paths and Saddle Points. *J. Phys. Chem. A* **2000**, *113* (22), 9978−9985.
(42) Henkelman, G.; Uberuaga, B. P.; Jónsson, H. A Climbing Image Nudged Elastic Band Method for Finding Saddle Points and Minimum Energy Paths. *J. Phys. Chem. A* **2000**, *113* (22), 9901−9904.
(43) Parija, A.; Liang, Y.; Andrews, J. L.; De Jesus, L. R.; Prendergast, D.; Banerjee, S. Topochemically De-Intercalated Phases of V_2O_5 as Cathode Materials for Multivalent Intercalation Batteries: A First-Principles Evaluation. *Chem. Mater.* **2016**, *28* (16), 5611−5620.
(44) Xiao, R.; Xie, J.; Luo, T.; Huang, L.; Zhou, Y.; Yu, D.; Chen, C.; Liu, Y. Phase Transformation and Diffusion Kinetics of V_2O_5 Electrode in Rechargeable Li and Mg Batteries: A First-Principle Study. *J. Phys. Chem. C* **2018**, *122* (3), 1513−1521.
(45) Sotoudeh, M.; Dillenz, M.; Döhn, J.; Hansen, J.; Dsoke, S.; Groß, A. Oxide Spinels with Superior Mg Conductivity. *Chem. Mater.* **2023**, *35* (12), 4786−4797.
(46) Kokalj, A. Computer Graphics and Graphical User Interfaces as Tools in Simulations of Matter at the Atomic Scale. *Comput. Mater. Sci.* **2003**, *28* (2), 155−168.
(47) Houdeville, R. G.; Black, A. P.; Ponrouch, A.; Palacín, M. R.; Fauth, F. Operando Synchrotron X-Ray Diffraction Studies on TiS_2: The Effect of Propylene Carbonate on Reduction Mechanism. *J. Electrochem. Soc.* **2021**, *168* (3), No. 030514.
(48) Adelhelm, P.; Sun, Y.; Åvall, G.; Wu, S.-H.; Ferrero, G. A.; Wang, H.; Mazzio, K.; Bianchini, M.; Baran, V.; Risse, S. Solvent Co-Intercalation in Layered Cathode Active Materials for Sodium-Ion Batteries *Res. Square* 2024 DOI: 10.21203/rs.3.rs-4564500/v1.
(49) Alvarez Ferrero, G.; Åvall, G.; Mazzio, K. A.; Son, Y.; Janßen, K.; Risse, S.; Adelhelm, P. Co-Intercalation Batteries (CoIBs): Role of TiS_2 as Electrode for Storing Solvated Na Ions. *Adv. Energy Mater.* **2022**, *12* (47), No. 2202377.
(50) Baur, W. H. The Geometry of Polyhedral Distortions. Predictive Relationships for the Phosphate Group. *Acta Crystallogr., Sect. B:Struct. Sci.* **1974**, *30* (5), 1195−1215.
(51) Robinson, K.; Gibbs, G. V.; Ribbe, P. H. Quadratic Elongation: A Quantitative Measure of Distortion in Coordination Polyhedra. *Science* **1971**, *172* (3983), 567−570.
(52) Wong, J.; Lytle, F. W.; Messmer, R. P.; Maylotte, D. H. K-Edge Absorption Spectra of Selected Vanadium Compounds. *Phys. Rev. B* **1984**, *30* (10), No. 5596.
(53) Tanaka, T.; Yamashita, H.; Tsuchitani, R.; Funabiki, T.; Yoshida, S. X-Ray Absorption (EXAFS/XANES) Study of Supported Vanadium Oxide Catalysts. Structure of Surface Vanadium Oxide Species on Silica and γ-Alumina at a Low Level of Vanadium Loading. *J. Chem. Soc. Faraday Trans. 1* **1988**, *84* (9), 2987−2999.
(54) Mansour, A. N.; Smith, P. H.; Baker, W. M.; Balasubramanian, M.; McBreen, J. A Comparative in Situ X-Ray Absorption Spectroscopy Study of Nanophase V_2O_5 Aerogel and Ambigel Cathodes. *J. Electrochem. Soc.* **2003**, *150* (4), No. A403.
(55) Nabavi, M.; Taulelle, F.; Sanchez, C.; Verdaguer, M. Xanes and 51V NMR Study of Vanadium-Oxygen Compounds. *J. Phys. Chem. Solids* **1990**, *51* (12), 1375−1382.
(56) Silversmit, G.; Depla, D.; Poelman, H.; Marin, G. B.; De Gryse, R. Determination of the V2p XPS Binding Energies for Different Vanadium Oxidation States (V^{5+} to V^{0+}). *J. Electron Spectrosc. Relat. Phenom.* **2004**, *135* (2), 167−175.
(57) Ho, C.; Raistrick, I. D.; Huggins, R. A. Application of A-C Techniques to the Study of Lithium Diffusion in Tungsten Trioxide Thin Films. *J. Electrochem. Soc.* **1980**, *127* (2), 343−350.
(58) Casas-Cabanas, M.; Roddatis, V. V.; Saurel, D.; Kubiak, P.; Carretero-González, J.; Palomares, V.; Serras, P.; Rojo, T. Crystal Chemistry of Na Insertion/Deinsertion in $FePO_4$−$NaFePO_4$. *J. Mater. Chem.* **2012**, *22* (34), 17421−17423.
(59) Adams, K.; González, A. F.; Mallows, J.; Li, T.; Thijssen, J. H. J.; Robertson, N. Facile Synthesis and Characterization of $Bi_{13}S_{18}I_2$ Films as a Stable Supercapacitor Electrode Material. *J. Mater. Chem. A* **2019**, *7* (4), 1638−1646.

(60) Yamaura, J.-I.; Isobe, M.; Yamada, H.; Yamauchi, T.; Ueda, Y. Low Temperature X-Ray Study of β-$A_xV_2O_5$. *J. Phys. Chem. Solids* **2002**, *63* (6), 957−960.
(61) Kim, D. J.; Ponraj, R.; Kannan, A. G.; Lee, H.-W.; Fathi, R.; Ruffo, R.; Mari, C. M.; Kim, D. K. Diffusion Behavior of Sodium Ions in $Na_{0.44}MnO_2$ in Aqueous and Non-Aqueous Electrolytes. *J. Power Sources* **2013**, *244*, 758−763.
(62) Anne, H. Understanding the Kinetic Limitations of NaFePO4 as Cathode Active Material for Na-Ion Batteries; Ph.D. Dissertation; Universidad del País Vasco, 2019. https://addi.ehu.es/handle/10810/32550.

https://doi.org/10.1021/acs.chemmater.5c01520
Chem. Mater. 2025, 37, 8649−8663